Agricultural and Forest Meteorology 349 (2024) 109962

Contents lists available at ScienceDirect

Agricultural and Forest Meteorology

journal homepage: www.elsevier.com/locate/agrformet

Multimodel ensemble estimation of Landsat-like global terrestrial latent heat flux using a generalized deep CNN-LSTM integration algorithm☆,☆☆

Xiaozheng Guo [a], Yunjun Yao [a,*], Qingxin Tang [b], Shunlin Liang [c], Changliang Shao [d], Joshua B. Fisher [e], Jiquan Chen [f], Kun Jia [a], Xiaotong Zhang [a], Ke Shang [g], Junming Yang [a], Ruiyang Yu [a], Zijing Xie [a], Lu Liu [a], Jing Ning [a], Lilin Zhang [h]

[a] *State Key Laboratory of Remote Sensing Science, Faculty of Geographical Science, Beijing Normal University, Beijing 100875, China*
[b] *School of Geography and Environment, Liaocheng University, Liaocheng 252000, China*
[c] *Department of Geographical Sciences, University of Hong Kong, Hongkong 999077, China*
[d] *State Key Laboratory of Efficient Utilization of Arid and Semi-arid Arable Land in Northern China, National Hulunber Grassland Ecosystem Observation and Research Station, Institute of Agricultural Resources and Regional Planning, Chinese Academy of Agricultural Sciences, Beijing 100081, China*
[e] *Schmid College of Science and Technology, Chapman University, University Drive, Orange, CA 92866, USA*
[f] *Department of Geography, Environment, and Spatial Sciences, Michigan State University, East Lansing, MI 48823, USA*
[g] *School of Space Information, Space Engineering University, Beijing 101416, China*
[h] *Faculty of Geo-Information and Earth Observation (ITC), University of Twente, AE Enschede 7500, the Netherlands*

ARTICLE INFO

Keywords:
Latent heat flux
Integration algorithm
CNN-LSTM
Landsat
High-spatial-resolution products

ABSTRACT

Accurate estimates of high-spatial-resolution global terrestrial latent heat flux (LE) from Landsat data are crucial for many basic and applied research. Yet current Landsat-derived LE products were developed using single algorithm with large uncertainties and discrepancies. Here we proposed a convolutional neural network-long short-term memory (CNN-LSTM)-based integrated LE (CNN-LSTM-ILE) framework that integrates five Landsat-derived physical LE algorithms, topography-related variables (elevation, slope and aspect) and eddy covariance (EC) observations to estimate 30-m global terrestrial LE. CNN-LSTM-ILE not only conserves good performance of LE estimation from pure deep learning (DL) algorithm, but partially inherits physical mechanism of the individual physical algorithms for improving the generalization of the integration algorithms for extreme cases. CNN-LSTM is an algorithm that combines two deep learning structures (CNN and LSTM) to effectively utilize the spatial and temporal information contained in the forcing inputs. The data were collected from 190 globally distributed EC observations from 2000 to 2015 and were provided by FLUXNET. The cross-validation results indicated that the CNN-LSTM integration algorithm improved the LE estimates by reducing the root mean square error (RMSE) of 5–8 W/m^2 and increasing Kling-Gupta efficiency (KGE) of 0.05–0.16 when compared with the individual LE algorithms and the results of three other machine learning integration algorithms (multiple linear regression, MLR; random forest, RF; and deep neural networks, DNN). The CNN-LSTM integration algorithm had highest KGE (0.81) and R^2 (0.66) compared to ground-measured and was applied to generate the Landsat-like regional and global terrestrial LE. An innovation of our strategy is that the CNN-LSTM-ILE model integrates pixel proximity effects and daily LE variations to enhance the accuracy of 16-day LE estimations. This approach can produce a more reliable Landsat-like global terrestrial LE product to improve the representativeness of heterogeneous regions for monitoring hydrological variables.

1. Introduction

The terrestrial latent heat flux (LE) is a key variable in land surface energy and hydrological processes, as well as for management of natural resources and ecosystem modeling (Allen et al., 1998; Fisher et al., 2017; Kool et al., 2014; Liang et al., 2010; Yao et al., 2017a). The accurate estimation of LE remains challenging due to the large heterogeneity of the land surfaces and complex forcing mechanisms (Fisher et al., 2017;

☆ Agricultural and Forest Meteorology☆☆ March 8, 2023

* Corresponding author.
E-mail address: boyyunjun@163.com (Y. Yao).

https://doi.org/10.1016/j.agrformet.2024.109962
Received 12 March 2023; Received in revised form 9 December 2023; Accepted 4 March 2024

Kalma et al., 2008; Li et al., 2009; Tang et al., 2010; Wang and Dickinson 2012). Eddy covariance (EC) flux towers represent the gold standard in ground-based LE estimation, but it still has large uncertainty as a reference data to simulate regional LE, especially in areas where the landscape heterogeneity are high (Baldocchi, 2008; Kalma et al., 2008). This may be attributed to the fact that EC have typical 20 % errors in LE measurement and topography (*e.g.*, elevation, slope and aspect) affects the redistribution of solar energy, surface water and microclimate factors that directly controls terrestrial LE (Shang et al. 2021). Additionally, the distribution of EC flux tower sites is sparse and cannot represent the LE on a large scale (Kessomkiat et al., 2013; Kustas and Anderson 2009; Liu et al., 2016; Perez-Priego et al., 2017; Yao et al., 2015).

Satellite Remote Sensing has provided an effective approach to produce spatially continuous LE products over large areas because it can obtain terrestrial information with broad spatial coverage (*e.g.*, normalized difference vegetation index, NDVI; fractional vegetation cover, FVC; land surface temperature, LST; and surface net radiation, R_n) (Anderson et al., 2008; Fisher et al., 2008; Fisher et al., 2017; Mu et al., 2007; Mu et al., 2011; Yao et al., 2013). Since the launch of Landsat-4 in 1982, the multispectral Landsat sensors acquire a quantity of data that can be used to estimate LE at high spatial resolution (30 m) and reasonable temporal resolution (16 day) (Wulder et al., 2019). Accurate simulations of LE at Landsat-like scale are critical for monitoring field-level water resources and indirectly evaluating coarse-resolution LE products (Yao et al., 2017a). Consequently, various Landsat-based LE models had been widely used, which can be divided into two categories (1) temperature -based models (Allen et al., 2007; Anderson et al., 1997; McVicar and Jupp, 2002; Norman et al., 1995; Yang and Shang, 2013; Yao et al., 2017b) and (2) vegetation-based models (Amazirh et al., 2017; Fisher et al., 2008; Fisher et al., 2020; McCabe et al., 2017; Ke et al., 2017; Khaldi et al., 2014). Temperature-based models typically calculate LE as a residual of the surface energy balance and use LST to simulate the sensible heat flux (H). Temperature-based models, such as Surface Energy Balance Algorithm for Land (SEBAL) model (Bastiaanssen et al., 1998a; Bastiaanssen et al., 1998b), Surface Energy Balance System (SEBS) (Su, 2002), Two-Source model coupled with Atmosphere-Land Exchange Inverse (ALEXI) model (Anderson et al., 1997) and Mapping Evapotranspiration with high Resolution and Internalized Calibration (METRIC) model (Allen et al., 2007), estimate LE via surface energy balance using visible and thermal Landsat data. Vegetation-based models use various eco-physiological constraints derived from remotely sensed vegetation indices to estimate LE. Vegetation-based models link LE to Landsat-derived vegetation parameters (*e.g.,* normalized difference vegetation index, NDVI; Leaf Area Index, LAI) and other meteorological variables (*e.g.,* relative humidity, RH; and air temperature, Ta) using empirical equations or process-based methods. These empirical equations are established through statistical methods or machine learning approaches, enabling the upscaling of LE values from eddy covariance (EC) flux tower sites to regional scales. Although these models can produce acceptable LE products using Landsat data, they still have considerable discrepancies and uncertainties in their LE estimations due to the different model parameters and model structures (Anderson et al., 2021; Ershadi et al., 2014; Khaldi et al., 2014). The discrepancies between these models are mainly due they are designed to satisfy different purposes, such as vegetation-based models are more suitable than temperature-based methods for rainforest where LE is tightly coupled to vegetation characteristics (Ershadi et al., 2014), but they cannot estimate exactly LE over irrigated vegetation.

Integrating satellite LE algorithms and ground-measured observations is an effective strategy to improve the accuracy of LE estimations because the integration methods can make full use of the merits of multiple LE algorithms and the prior information of ground-measured observations over different land cover types (Chen et al., 2015; Elnashar et al., 2021; Yao et al., 2014). Previous studies have demonstrated that statistical and machine learning integration methods are better than individual models for producing LE products (Feng et al., 2016; Yao et al., 2014; Yao et al., 2017a). For example, Yao et al. (2017a) applied a statistical Taylor skill integration (STS) method to integrate five LE models and generated a reliable global LE product with 30-m spatial resolution and found that the accuracy of the LE estimates based on the STS method improved by 3 % to 8 % compared to individual LE models. Kraft et al. (2021) introduced a hybrid hydrological model that combines machine learning and physical principles to effectively simulate global water cycle components, demonstrating its capability to enhance global hydrological modeling by integrating data-driven methods with traditional modeling frameworks. Unfortunately, these algorithms for integrating LE products did not engage a full use of the spatial and temporal information as the forcing inputs for improving LE estimates (Yao et al., 2021; Yuan et al., 2020). Integrating multiple LE models should consider more factors, such as the influence of adjacent pixels on the central pixel, or the effect of daily LE on the multi-day average LE. Clearly, a spatial and temporal integration framework to ensemble all available information from Landsat-derived physical models, EC observations and topography-related variables is required for improving regional and global LE estimation.

Deep convolutional neural network (CNN) and long short-term memory (LSTM), as state-of-the-art deep learning algorithms, have achieved great success in many applications (*e.g.*, precipitation forecasting, crop yield prediction, and air temperature estimates) because CNN can use convolutional layer or pooling layer to capture spatial-spectral information and LSTM can extract the temporal dependency of time series data through structure of forget gate, input gate and output gate. (Esteva et al., 2019; Guo et al., 2016; LeCun et al., 2015; Shen et al., 2020; Shi et al., 2020; Sun et al., 2019; Tsagkatakis et al., 2019; Zamani Joharestani et al. 2019). Substantial previous studies have illustrated the ability of CNN-LSTM in predicting a variety of land surface environmental variables (Chang and Luo, 2019; Shen et al., 2020). We are convinced that CNN-LSTM has great potential for estimating Landsat-like global terrestrial LE by integrating multiple Landsat-derived LE models, topography information and EC ground observations.

In this study, we proposed a deep CNN-LSTM-based integrated LE (CNN-LSTM-ILE) framework for integrating five Landsat-derived physical LE algorithms (RS-PM, SW, PT-JPL, MS-PT, and UMD-SEMI), topography-related variables (elevation, slope and aspect), and EC observations to improve Landsat-like global terrestrial LE estimations. Our objectives are to (1) develop a CNN-LSTM-ILE framework for integrating multiple LE algorithms; (2) evaluate the performance of the CNN-LSTM-ILE framework based on global long-term (2000–2015) EC observations from 190 EC flux tower sites and compare its performance with other integration algorithms; and (3) estimate Landsat-like global terrestrial LE with 30-m spatial resolution and 16-day temporal resolution using the CNN-LSTM-ILE framework.

2. Methodology

2.1. CNN-LSTM-ILE framework

The deep convolutional neural network-long short-term memory (CNN- LSTM)-based integrated LE (CNN-LSTM-ILE) framework that integrates five Landsat-derived physical LE algorithms, topography data and EC observations using a deep CNN-LSTM integration algorithm is shown in Fig. 1. First, the five Landsat-derived physical LE algorithms used the daily forcing data (Landsat and reanalysis data) to estimate LE. Second, the daily LE estimations using five physical algorithms (SW, MS-PT, PT-JPL, RS-PM and UMD-SEMI), topography-related variables (elevation, slope and aspect) and the corresponding training EC observations were extracted as input features for algorithm development. Third, the CNN-LSTM algorithm and three other machine learning algorithms (multiple linear regression, MLR; random forest, RF; and deep neural network, DNN) were used to integrate the input features to estimate the 16-day Landsat-like LE. Then, different integration

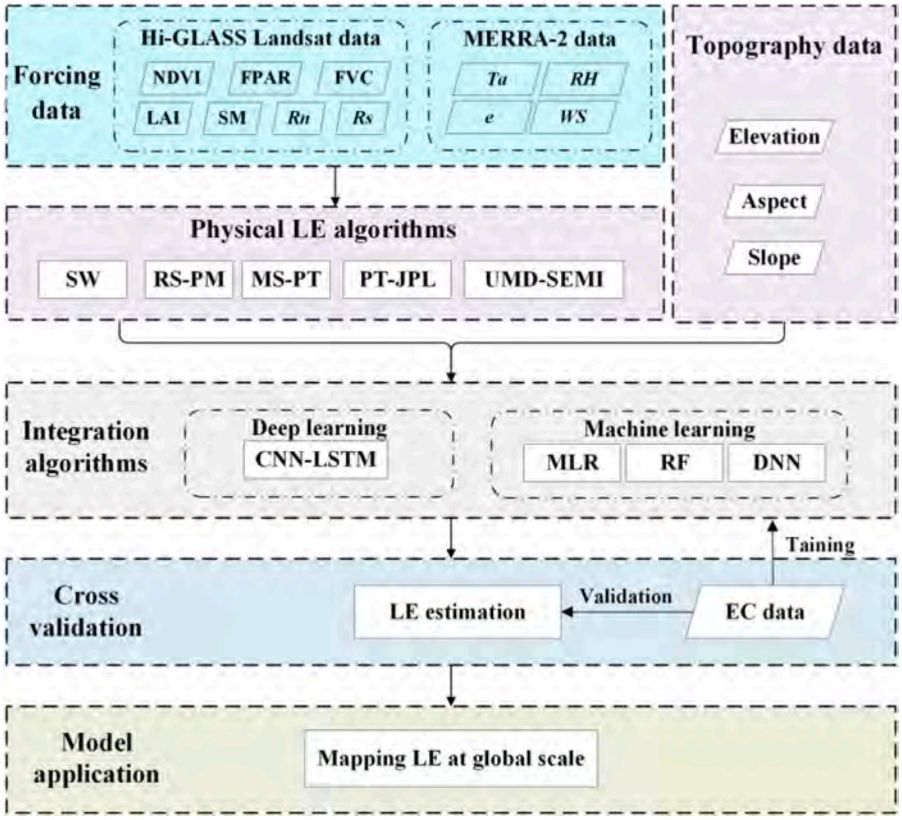

Fig. 1. Our CNN-LSTM-ILE framework integrates five Landsat-derived physical LE algorithms, topographic data and EC observations using a deep CNN-LSTM integration algorithm.

algorithms were evaluated by using the 16-day ground-observed LE based on the 10-fold cross validation method. Finally, based on the deep CNN-LSTM integration algorithm, we estimated Landsat-like global terrestrial LE with 16-day temporal resolution for 2013–2015.

2.2. Five landsat-derived physical LE algorithms

The daily LE values were estimated based on five classic physical LE algorithms that are driven by remote sensing data and meteorological variables. Previous studies showed that vegetation-based algorithms are superior to the temperature-based algorithms for estimating terrestrial LE (root mean square error (RMSE) of 18 W/m^2 for the vegetation-based algorithm *versus* 25 W/m^2 for the temperature-based algorithm) (Glenn et al., 2011). Thus, we only select five traditional vegetation based LE algorithms to estimate terrestrial LE in this study. Each of LE algorithm is described below.

(1) RS-PM LE algorithm. The Remote-Sensing-Based Penman–Monteith (RS-PM) LE algorithm was simplified from the PM algorithm described in (Mu et al., 2007). To reduce the effects of misclassification of plant functional types, RS-PM algorithm was revised as the invariant model parameters across different land cover types (Yuan et al., 2010). RS-PM algorithm can be computed as follows:

$$LE = \frac{\Delta(R_n - G) + \rho C_p VPD / r_a}{\Delta + \gamma(1 + r_s/r_a)} \tag{1}$$

where Δ is the slope of the saturation water vapor pressure curve; γ is the psychrometric constant; ρ is the density of the air; r_a is the aerodynamic resistance and r_s is the surface resistance. The forcing variables of the RS-PM LE algorithm include the air temperature (T_a), air relative humidity (*RH*) and vapor pressure (*e*), leaf area index (LAI) and land surface net radiation (R_n). To obtain r_s, we modified the moisture constraint (m_{VPD}) by setting VPD_{close} and VPD_{open} as 650 Pa and 2900 Pa for all ecosystem types, respectively.

$$m_{VPD} = \begin{cases} 1.0 & VPD \le VPD_{\text{open}} \\ \dfrac{VPD_{\text{close}} - VPD}{VPD_{\text{close}} - VPD_{\text{open}}} & VPD_{\text{open}} < VPD < VPD_{\text{close}} \\ 0.1 & VPD \ge VPD_{\text{close}} \end{cases} \tag{2}$$

where close refers to nearly complete inhibition and open refers to no inhibition to transpiration.

(2) SW LE algorithm. The Shuttleworth-Wallace dual-source (SW) LE algorithm separately considers vegetation transpiration and soil evaporation, and the individual LE components are calculated from the Penman–Monteith formula (Shuttleworth and Wallace 1985), which uses a scientific hypothesis of aerodynamic mixing arising at the canopy. The SW LE algorithm can be presented as:

$$LE = C_s LE_s + C_s LE_v \tag{3}$$

$$LE_s = \frac{\Delta(R_n - G) + \left(\rho C_p VPD - \Delta r_{as} R_{nc}\right)/(r_{aa} + r_{as})}{\Delta + \gamma[1 + r_{ss}/(r_{aa} + r_{as})]} \tag{4}$$

$$LE_v = \frac{\Delta(R_n - G) + \left[\rho C_p VPD - \Delta r_{ac}(R_{ns} - G)\right]/(r_{aa} + r_{ac})}{\Delta + \gamma[1 + r_{sc}/(r_{aa} + r_{ac})]} \tag{5}$$

$$C_s = \frac{1}{1 + [R_s R_a/(R_c(R_s + R_a))]} \tag{6}$$

$$C_v = \frac{1}{1 + [R_c R_a/(R_s(R_c + R_a))]} \tag{7}$$

$$R_a = (\Delta + \gamma) r_{aa} \tag{8}$$

$$R_s = (\Delta + \gamma) r_{as} + r_{ss}\gamma \tag{9}$$

$$R_c = (\Delta + \gamma) r_{ac} + r_{sc}\gamma \tag{10}$$

Where C_s and C_v are the surface resistance coefficients for soil and vegetation, respectively. LE_s and LE_v are the soil evaporation and vegetation transpiration, R_{ns} and R_{nc} are R_n into soil and vegetation, respectively. r_{aa} is aerodynamic resistances from vegetation canopy. r_{as} and r_{ac} are aerodynamic resistances from the soil surface to canopy and leaf to canopy height, respectively. r_{ss} and r_{sc} are the surface resistance for soil and vegetation, respectively. The SW LE algorithm requires the wind speed (WS), *e, T_a* LAI, soil moisture (SM) and R_n. We used SM to calculate r_{ss} and it can be expressed as,

$$r_{ss} = \exp(8.206 - 4.255\mathrm{SM}) \tag{11}$$

(3) PT-JPL LE algorithm. The Priestley-Taylor-Based (PT-JPL) LE algorithm was designed by Fisher et al. (2008) based on the Priestley-Taylor algorithm. The LE algorithm uses the atmospheric and eco-physiological variables to characterize the soil and vegetation constraints by reducing the model input parameters. PT-JPL downscales the potential LE to actual LE using the Fraction of Absorbed Photosynthetically Active Radiation (FPAR), vapor pressure deficit (VPD), *RH*, LAI and NDVI. The PT-JPL LE algorithm can be presented as:

$$LE = LE_s + LE_c + LE_i \tag{12}$$

$$LE_s = \alpha\left[RH^4 + \left(1 - RH^4\right)RH^{VPD}\right]\frac{\Delta}{\Delta + \gamma}(R_{ns} - G) \tag{13}$$

$$LE_c = \alpha\left(1 - RH^4\right)f_g f_T f_M \frac{\Delta}{\Delta + \gamma} R_{nc} \tag{14}$$

$$LE_i = \alpha RH^4 \frac{\Delta}{\Delta + \gamma} R_{nc} \tag{15}$$

Where LE_s, LE_c and LE_i are soil evaporation, vegetation transpiration, and evaporation of canopy interception. f_g, f_T and f_M are green canopy fraction, plant temperature constraint and plant moisture constraint. The input variables of PT-JPL LE algorithm include *T_a, e, RH, R_n*, FPAR, LAI and NDVI.

(4) MS-PT LE algorithm. The Modified Satellite-Based Priestley-Taylor (MS-PT) LE algorithm was developed by Yao et al. (2013) and uses the apparent thermal inertia (ATI) calculated from the diurnal temperature range (DT) to reflect the soil moisture constraints. The MS-PT algorithm estimates the LE via four components, namely, vegetation canopy transpiration (LE_v), saturated soil evaporation (LE_{as}), unsaturated soil evaporation (LE_s) and vegetation interception evaporation (LE_{ic}). The MS-PT LE algorithm can be presented as:

$$LE = LE_v + LE_{as} + LE_s + LE_{ic} \tag{16}$$

$$LE_v = \alpha(1 - f_{\mathrm{wet}})f_c f_T \frac{\Delta}{\Delta + \gamma} R_{nc} \tag{17}$$

$$LE_{as} = \alpha f_{\mathrm{wet}} \frac{\Delta}{\Delta + \gamma}(R_{ns} - G) \tag{18}$$

$$LE_s = \alpha(1 - f_{\mathrm{wet}})f_{sm} \frac{\Delta}{\Delta + \gamma}(R_{ns} - G) \tag{19}$$

$$LE_{ic} = \alpha f_{\mathrm{wet}} \frac{\Delta}{\Delta + \gamma} R_{nc} \tag{20}$$

$$f_{sm} = \left(\frac{1}{DT}\right)^{DT/DT_{max}} \tag{21}$$

$$f_{wet} = f_{sm}^4 \tag{22}$$

The inputs of the MS-PT algorithm include DT and T_a, NDVI and R_n.

(5) UMD-SEMI LE algorithm. The Semi-empirical Penman LE algorithm of the University of Maryland (UMD-SEMI) was proposed by Wang et al. (2010) and is based on the basic Penman formula (Penman 1948). The UMD-SEMI LE algorithm considers the influence of SM on LE by introducing the air relative humidity deficit (RHD). The UMD-SEMI LE algorithm can be presented as:

$$LE_E = \frac{\Delta}{\Delta + \gamma} \cdot R_s \cdot [a_1 + a_2 \cdot NDVI + RHD \cdot (a_3 + a_4 \cdot NDVI)] \tag{23}$$

$$LE_A = \frac{\gamma}{\Delta + \gamma} \cdot WS \cdot VPD \cdot [a_5 + RHD \cdot (a_6 + a_7 NDVI)] \tag{24}$$

$$LE = a_8 \cdot (LE_E + LE_A) + a_9 \cdot (LE_E + LE_A)^2 \tag{25}$$

$$RHD = 1 - RH \tag{26}$$

Where a_i (i=1…,9) are empirical coefficient. This algorithm relates the incident solar radiation (R_s), VPD, T_a, RH and NDVI to the LE variability and introduces the contribution of wind speed (WS) to LE.

2.3. Deep CNN-LSTM integration algorithm

Convolutional neural network (CNN) was proposed to handle multiple arrays (LeCun et al. 1998), such as satellite images comprised of several 2D arrays. A CNN is composed of convolutional layers and pooling layers with four advantages (including pooling, shared weights, local connections and multi-layer use) to process row data (LeCun et al., 2015). These advantages give CNN an excellent ability to extract crucial spatial feature from the row data. Therefore, CNN exhibit first-class performance in the field of image segmentation and recognition. For the integration of Landsat-derived LE products, the LE value of each Landsat pixel is related to the LE values of the surrounding pixels, and CNN can capture the spatial feature information of LE variations. The spatial relationships for the LE value of the target pixel and the LE values of the surrounding pixels are obtained through various perceptual domains of multi-layer CNN. The CNN can be described as follows:

$$h_{i,j} = \mathrm{relu}\left[\sum_{k=1}^{K}\left(h_{i-1,k} * w_{i,kj}\right) + b_{i,j}\right] \tag{27}$$

$$h'_{i,j}(l) = \mathrm{relu}\left[h_{i,j}(ml), \ldots, h_{i,j}(ml + n - 1)\right] \tag{28}$$

where $h_{i,j}$ is the *j* feature map from the *i* convolutional layer, $w_{i,kj}$ is the kernel, *K* is the number of feature maps, *m* is the step number, and *n* is the number of outputs. “relu” represents the activation function of the CNN and can be written as follows:

$$f(x) = \begin{cases} 0 \; for \; x < 0 \\ x \; for \; x \geq 0 \end{cases} \tag{29}$$

Long short-term memory (LSTM) is a variant of a recurrent neural network (RNN), which is a type of artificial neural network that can process time-sequential data (Hochreiter and Schmidhuber 1997; Rumelhart et al., 1986). To process sequential data, such as language and time series data, RNN is a better choice. However, RNN has a vanishing gradient problem that decreases their performance (Graves and Schmidhuber 2005). To improve the performance of RNN, the LSTM was proposed by Hochreiter and Schmidhuber (1997) to learn the long-term dependency of sequential data. LSTM includes three gates (input gates, output gates and forget gates) to extract information. After LSTM obtains the input data $x = [x_1, \ldots, x_N]$, the input gate i_k determines the rate of the input information. $\tilde{c}_k$ is reserved to this cell state. Then, the forget gate f_k decides how much information from the last cell state is preserved in this one. Finally, the output gate o_k can provide new information for the next cell state c_k. The formulas for an LSTM are as follows:

$$f_k = \sigma\left(W_{fx}x_k + W_{fh}h_{k-1} + b_f\right) \tag{30}$$

$$i_k = \sigma(W_{ix}x_k + W_{ih}h_{k-1} + b_i) \tag{31}$$

$$o_k = \sigma\left(W_{ox}x_j + W_{oh}h_{k-1} + b_o\right) \tag{32}$$

$$\widetilde{c}_k = \tanh\left(W_{cx}x_j + W_{ch}h_{k-1} + b_c\right) \tag{33}$$

$$c_k = f_k * c_{k-1} + i_k * \widetilde{c}_k \tag{34}$$

$$h_k = o_k * \tanh(c_k) \tag{35}$$

$$\sigma(x) = \frac{1}{1+e^{-x}} \tag{36}$$

$$\tanh(x) = \frac{e^x - e^{-x}}{e^x + e^{-x}} \tag{37}$$

where W_{fx}, $W_{ix}x_k$, $W_{ox}x_j$, $W_{cx}x_j$, $W_{fh}h_{k-1}$, $W_{ih}h_{k-1}$, $W_{oh}h_{k-1}$, and $W_{ch}h_{k-1}$ represent the weight matrices and b_f, b_i, b_o, and b_c represent the biases. For Landsat-derived LE integration, the LSTM can obtain the time dependence of LE information from the daily LE values and provide 16-day LE results.

To find the temporal and spatial relationships among the EC observations and Landsat-derived LE products, CNN and LSTM were used to capture the spatial characteristics and time dependences, respectively. Thus, a CNN-LSTM-ILE framework was constructed by combining CNN with LSTM to integrate the Landsat-derived LE algorithms, topography and EC observations. Fig. 2 shows the framework of the CNN-LSTM integration algorithm. The CNN-LSTM algorithm has two modules: 1) the CNN spatial information extraction module and 2) the LSTM temporal dependency information module. The CNN module (including convolutional layers and pooling layers) was used to extract the information that is related to the LE values of subpixel center points from the Landsat-derived LE products. For LE estimations, each LE pixel value is not independent and is associated with the surrounding pixel values. Similarly, the LSTM was used to obtain the relationships among the LE products at different times to improve the 16-day LE estimates.

To implement the CNN-LSTM integration algorithm, we extracted 11 $\times$ 11 pixels (330$\times$330 m) that were centered on each EC flux tower site (Fig. 3). This provides a conservative and consistent comparison, though a more rigorous approach would include a detailed tower footprint analysis and matchup (Fisher et al., 2020). Considering that the pixels contain 16 daily Landsat-derived LE values (RS-PM, SW, PT-JPL, MS-PT and UMD-SEMI) and topography-related variables (elevation, aspect and slope), the shape of the input features for the CNN-LSTM algorithm is $16 \times 8 \times 11 \times 11$ (day $\times$ features $\times$ shape of pixels). Thus, the training datasets (input features and EC observations) for the CNN-LSTM algorithm were established.

Fig. 4 shows the structure and hyperparameters of the deep CNN-LSTM integration algorithm. It characterizes the entire process of producing 16-day LE estimates from the input features to the results. The rounded rectangles represent the input features, intermediate results and LE estimates. The rounded rectangles represent the shapes of the input features and feature types. The rectangles indicate the layers of the deep CNN-LSTM integration algorithm and their parameters. Convolution2D is the convolutional layer, which is followed by the convolution kernel size and number of output layers. The global average pooling layer obtains the average value of each layer. The concatenate layer connects these two vectors into one.

2.4. Other integration algorithms

(1) Multiple linear regression (MLR). MLR is a statistical algorithm that obtains the simple linear relationships between several input features and the target variable by using the least squares algorithm. Previous studies have reported that linear regression can express the relationship between multi-model LE estimates and actual LE (Shang et al., 2020; Yao et al., 2017a). The MLR algorithm is simple and efficient but cannot simulate nonlinear relationships.

(2) Random forest (RF) model. RF was proposed by Breiman (2001) and is an ensemble learning algorithm that is used for classification and regression. The RF model consists of multiple decision trees, and each tree is trained by using a bootstrap sampling algorithm. For the regression task, the result of the RF is the average prediction of the individual decision trees. Due to the ensemble algorithm of the RF, it has a strong simulation ability and can effectively avoid overfitting.

(3) Deep neural network (DNN). DNN was developed based on multilayer perceptron (MLP) (Hornik 1991). The difference between DNN and MLP is that DNN has more layers (ten or more layers) and effective nonlinear fitting abilities. DNN uses the backpropagation

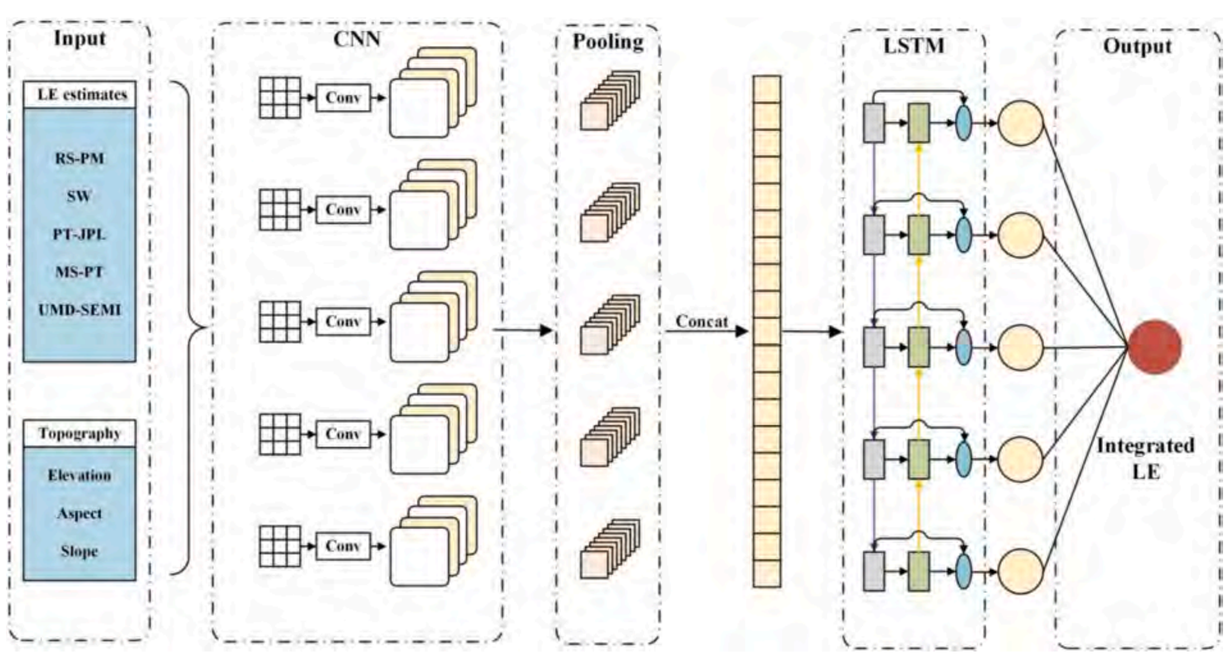

Fig. 2. Framework of the CNN-LSTM integration algorithm.

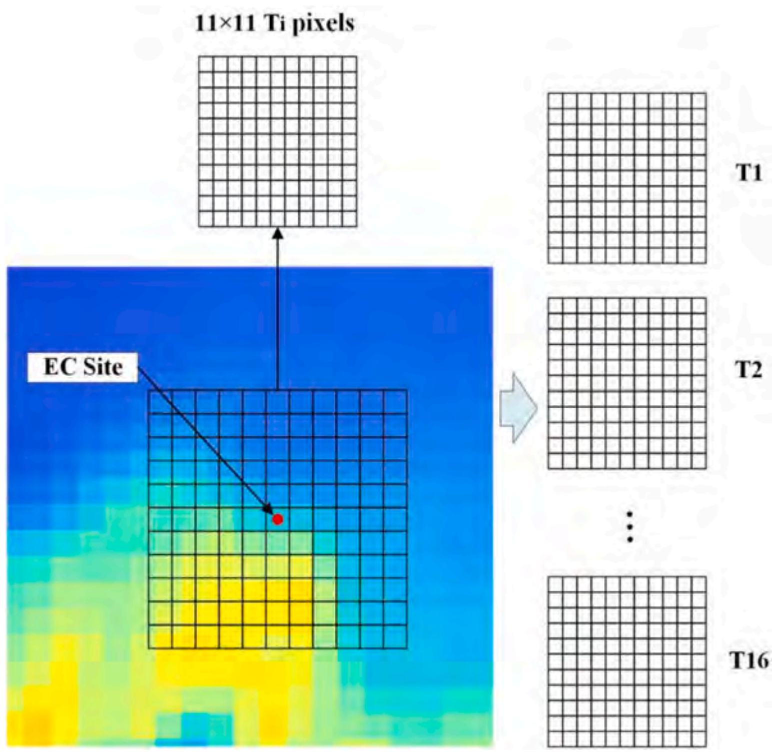

Fig. 3. Diagram of pixel data extraction.

algorithm, which is the key factor that improves the model training efficiency, to optimize the model parameters. Overfitting is a critical issue for DNN because DNN has a very large number of parameters. Therefore, we used the dropout algorithm to avoid overfitting. The DNN contains input layers, hidden layers and an output layer.

2.5. Evaluation methods

We used the coefficient of determination (R^2), root mean square error (RMSE), bias and Kling-Gupta efficiency (KGE) to evaluate the performances of different algorithms. R^2 is used to obtain the consistency between estimations and observations by calculating their correlation coefficient; RMSE represents the closeness between estimations and observations; bias quantifies the difference between estimations and observations; and KGE is used to comprehensively evaluate the algorithm performance (Gupta et al., 2009). The KGE combines the correlation coefficient (r), mean value ratio (β) and relative variability ratio (α) to represent the algorithm performance. The mathematical equations of the performance metrics can be expressed as follows:

$$\mathrm{RMSE} = \sqrt{\frac{1}{n}\sum_{i=1}^{n}(X_i - Y_i)^2} \tag{38}$$

$$\mathrm{Bias} = \frac{\sum_{i=1}^{n}(X_i - Y_i)}{n} \tag{39}$$

$$\mathrm{R}^2 = \left(\frac{\sum_{i=1}^{n}(X_i - \overline{X})(Y_i - \overline{Y})}{\sqrt{\sum_{i=1}^{n}(X_i - \overline{X})(Y_i - \overline{Y})}}\right)^2 \tag{40}$$

$$\mathrm{KGE} = 1 - \sqrt{(r-1)^2 + \left(\frac{\sigma_e}{\sigma_o} - 1\right)^2 + \left(\frac{\mu_e}{\mu_o} - 1\right)^2} \tag{41}$$

Where X_i and Y_i are the estimated and observed LE, respectively; $\overline{X}$ and $\overline{Y}$ are the average of X_i and Y_i and n is the total number of the data, σ_e is the standard deviation of the estimations, σ_o is the standard deviation of the observations, μ_e is the average of the estimations and μ_o is the average of the observations.

3. Data

3.1. Eddy covariance observations

The LE algorithms were integrated and evaluated using a long-term dataset of EC observations. The EC observations were provided by FLUXNET (https://fluxnet.org/), which integrated the different networks, including AmeriFlux, ChinaFlux, AsiaFlux, LathuileFlux, Asian Automatic Weather Station Network (ANN) Project, Chinese Ecosystem Research Network (CERN) and the work of individual principal investigators (PIs). We used 190 global EC flux tower sites from FLUXNET that are mainly distributed in America, Europe and East Asia, with only two flux tower sites in Australia, five flux tower sites in South America and two flux tower sites in Africa (Fig. 5). The EC flux tower sites cover eight land cover types, including cropland (CRO, 27 towers); deciduous broadleaf forest (DBF, 25 towers); evergreen broadleaf forest (EBF, 14 towers); evergreen needleleaf forest (ENF, 55 towers); grassland (GRA, 47 towers); mixed forest (MF, 7 towers); savanna (SAW, 5 towers); and shrubland (SHR, 10 towers). These ground-measured data span the period from 2000 to 2015 and recorded one or more growing seasons.

The FLUXNET EC observations consist of half-hourly or hourly soil heat flux (G), sensible heat flux (H), incident solar radiation (R_s), R_n and LE data. The hourly or half-hourly LE, H, G and the meteorological variables were aggregated into daily means using the gap-filling method proposed by (Reichstein et al., 2005). If more than 25 % of the data were missing on a given day, the values of that day were considered missing. Since the EC method has an energy imbalance problem, we used the formula proposed by Twine et al. (2000) to correct the ground-measured LE. The formula can be written as:

$$LE_{\mathrm{cor}} = (R_n - G)/(H + LE) \times LE \tag{42}$$

where LE_{cor} is the corrected LE.

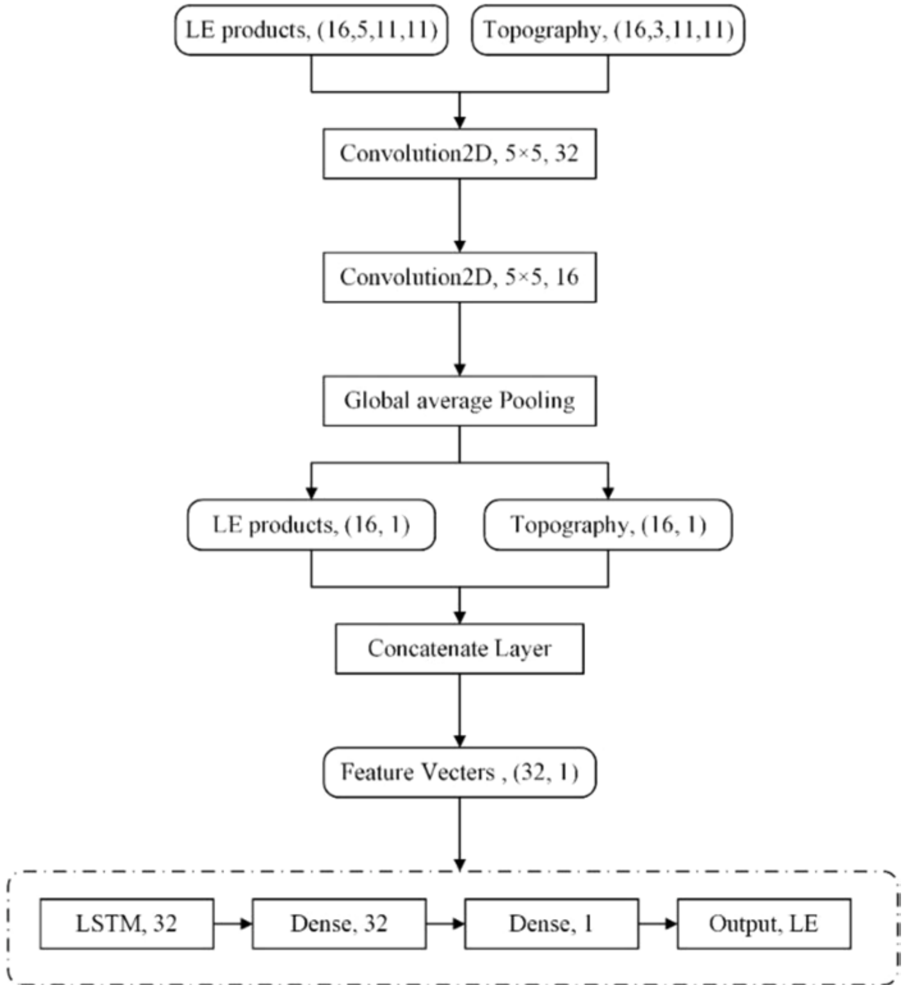

Fig. 4. Structure of the deep CNN-LSTM integration algorithm.

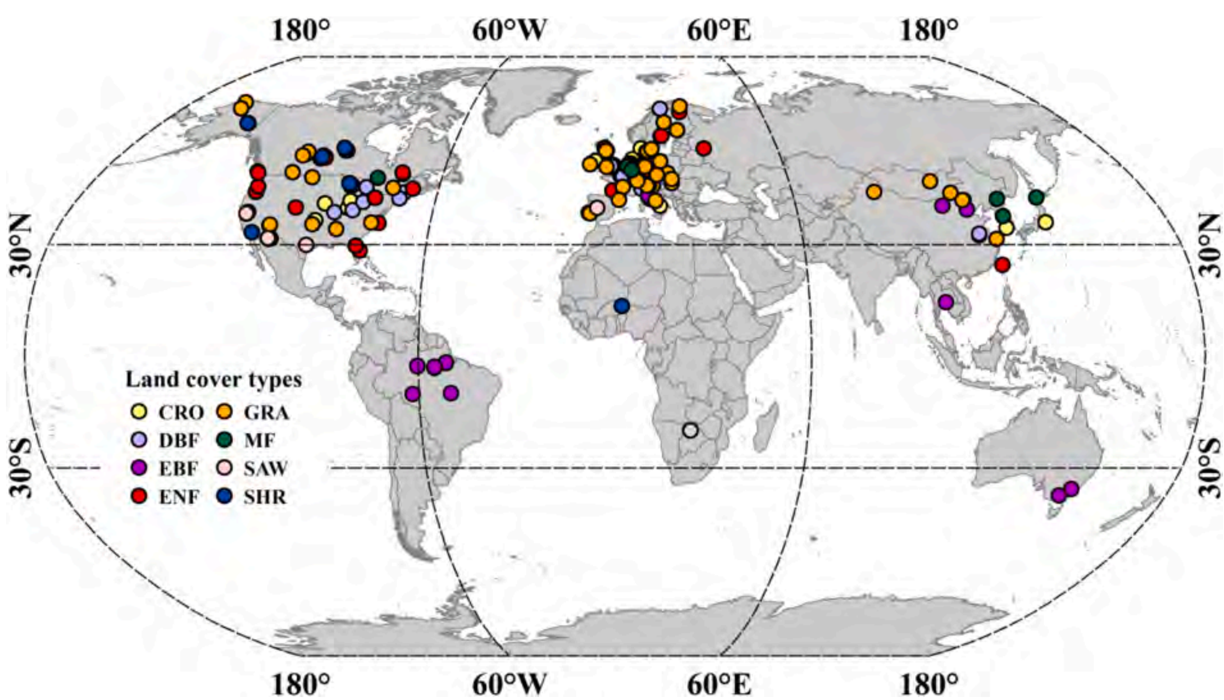

Fig. 5. The distribution of 190 EC flux tower sites for different land cover types.

We assessed the performance of the CNN-LSTM-ILE framework by using a 10-fold cross-validation method. The EC observations were stratified into 10 folds and each fold contained 10 % of the EC observations (Jung et al., 2011). Entire sites were assigned to each fold. A total of 91,125 site-16-days of EC data were used, randomly divided into 10 parts according to the spatial distribution and land cover types. The LE values for each of the 10 parts are estimated based on the trained algorithm by using the remaining nine parts.

3.2. Satellite and reanalysis data

Satellite and reanalysis data to drive five physical LE algorithms are listed in Table 1. The datasets include NDVI, fractional vegetation cover (FVC), LAI, R_s, R_n, SM and fraction of absorbed photosynthetically active radiation (FAPAR) from High-spatial-resolution Global LAnd Surface Satellite (Hi-GLASS) products and meteorological data. We used the daily Hi-GLASS NDVI product from Landsat data with a 30 m spatial resolution. This product was generated using the Savitzky–Golay (SG) method, as detailed in Lin et al. (2022).. The Hi-GLASS daily LAI and FPAR products with 30 m spatial resolution generated by the ensemble multiscale filter (EnMsF) approach were also used to drive LE algorithms (Jin et al., 2019; Jin et al., 2022). We also used the daily Hi-GLASS FVC product with 30 m spatial resolution through integrated use of Landsat 8 and Gaofen 2 data (Song et al., 2022). Additionally, both the daily Hi-GLASS SM R_s, and R_n products with 30 m spatial resolution were also used to estimate daily LE. The ensemble learning method was applied to generate daily Hi-GLASS SM product from Landsat data (Zhang et al., 2022) and the daily Hi-GLASS R_s and R_n products were yielded using RF model (Jiang et al., 2023).

When estimating regional and global terrestrial LE, the five Landsat-derived physical LE algorithms were driven by daily Modern-Era Retrospective Analysis for Research and Applications, version 2 (MERRA-2) meteorological data with spatial resolution of 0.5°× 0.625°. MERRA-2 variables used in this study include *Ta, DT, RH, e*, and *WS* (Gelaro et al., 2017). To match Landsat pixels, we used the algorithm developed by Zhao et al. (2005) to interpolate coarse-resolution MERRA-2 data to 30 m Landsat pixels. Theoretically, this interpolation algorithm enhances the accuracy of meteorological data for each 30 m pixel because the four MERRA-2 cells surrounding a given pixel remove sharp variations from one side of a MERRA-2 boundary to the other using a cosine function (Zhao et al., 2005).

3.3. Topography data

We used the Advanced Spaceborne Thermal Emission and Reflection Radiometer (ASTER) data (https://asterweb.jpl.nasa.gov/gdem.asp) as the topography information to improve the robustness of the CNN-LSTM-ILE framework. The ASTER Digital Elevation Model (DEM) has a 30-m spatial resolution that is consistent with the spatial resolution of the Landsat-derived LE products. It spans from 83° north latitude to 83° south latitude, which encompasses 99 % of the Earth's landmass. The Ministry of Economy, Trade, and Industry (METI) of Japan and the United States National Aeronautics and Space Administration (NASA) jointly released ASTER DEM version 3 on August 5, 2019. The ASTER DEM version 3 has been processed to fill data voids, and it has higher precision. The elevation, aspect and slope information were extracted from the ASTER DEM data using ArcGIS v10.7 software.

Table 1
Description of the satellite and reanalysis data.

Products	Spatial Resolution	Variables acquired	Refs.
MERRA-2 reanalysis product	0.5°× 0.625°	*RH, WS, Ta, e*	Gelaro et al. (2017)
Hi-GLASS vegetation products	30m	NDVI, LAI, FPAR, FVC	Lin et al. (2022), Jin et al. (2019), Jin et al. (2022), Song et al. (2022)
Hi-GLASS radiation products	30m	R_s, R_n	Jiang et al. (2023)
Hi-GLASS soil products	30m	SM	Zhang et al. (2022)

4. Results

4.1. Validation of five landsat-derived physical LE algorithms

The estimated daily LE using five Landsat-derived physical algorithms were validated based on the EC observations at 190 flux tower sites for different land cover types. Fig. 6 shows that the five Landsat-derived physical LE algorithms exhibit large discrepancies among the different land cover types at flux tower site scale. For the CRO, DBF and SHR flux tower sites, the UMD-SEMI algorithm has the highest KGE of more than 0.74 and R^2 of more than 0.54 (p < 0.01) and the lowest RMSE of less than 31 W/m^2 compared to the other LE algorithms. For the GRA flux tower sites, the MS-PT algorithm exhibits the smallest RMSE (25.9 W/m^2) and bias (0.6 W/m^2). The MS-PT LE algorithm also exhibits the highest KGE of more than 0.72 and R^2 of more than 0.51 (p < 0.01),

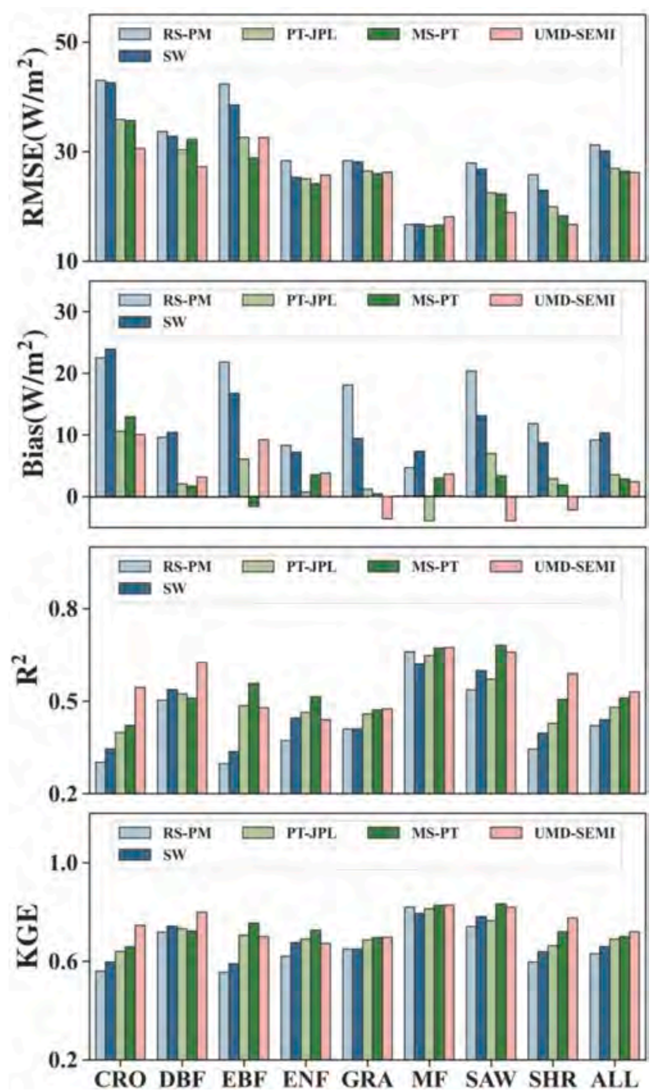

Fig. 6. Bar graphs of the statistics (KGE, R^2, bias and RMSE) of the comparisons between the daily LE from five physical LE algorithms and ground-measured data at 190 EC flux tower sites for different land cover types.

with a RMSE of less than 24.2 W/m^2 for both the EBF and ENF flux tower sites. For the SAW flux tower sites, the PT-JPL algorithm exhibits a higher R^2 (0.67) and bias (5 W/m^2) than the other four LE algorithms, whereas the SW LE algorithm exhibits better KGE (0.83) and R^2 (0.69, $p < 0.01$). According to the KGE (0.83) and R^2 (0.65, $p < 0.01$) values, the accuracy of the RS-PM LE algorithm is the highest for all the MF flux tower sites and it has a smaller RMSE (16.5 W/m^2).

Comparison of the ground-measured and estimated 16-day composited LE estimations for the different land cover types shows similar performance with daily LE estimations (Fig. 7). The UMD-SEMI LE algorithms have the highest KGE of more than 0.75 for the CRO and SHR flux tower sites. For EBF and ENF flux tower sites, the MS-PT LE algorithm shows better performance. According to RMSE, the RS-PM LE algorithm has highest accuracy. The PT-JPL and SW LE algorithms have better performance for SAW and DBF, respectively. This indicates that 16-day composited LE estimations has better accuracy than daily LE estimations and no single Landsat-derived physical LE algorithm can yield best LE estimation for all land cover types.

Overall, all five Landsat-derived physical LE algorithms provided reasonable 16-day LE estimations for all land cover types, with KGE ranging from 0.65 to 0.74, R^2 ranging from 0.43 to 0.54 ($p < 0.01$), bias ranging from 2.2 W/m^2 to 12.1 W/m^2 and RMSE ranging from 25.1 W/m^2 to 29.8 W/m^2 (Fig. 8). Generally, the UMD-SEMI LE algorithm shows the best performance with the highest KGE and R^2 values and lowest RMSE and is followed by the MS-PT, PT-JPL, SW and RS-PM LE algorithms. Compared with the worst-performing RS-PM algorithm, the UMD-SEMI algorithm reduces the RMSE by 4.7 W/m^2 and increases the KGE by approximately 0.10 and R^2 by 0.11. In general, the resistance-based LE algorithms (SW and RS-PM) have large biases due to the complex physical mechanisms and accumulated errors due to excessive numbers of input variables. In contrast, the PT-based LE algorithms (MS-PT and PT-JPL) exhibit higher accuracies in their LE estimations than the SW and RS-PM algorithms, which is due to their partitioning of the total LE and the smaller errors present in the required inputs (Ershadi et al., 2014; Fisher et al., 2005). Since the UMD-SEMI LE algorithm has been calibrated using EC ground observations at 64 flux tower sites across globally different land cover types, it obtains the best performance for LE estimations when compared to the other four LE algorithms.

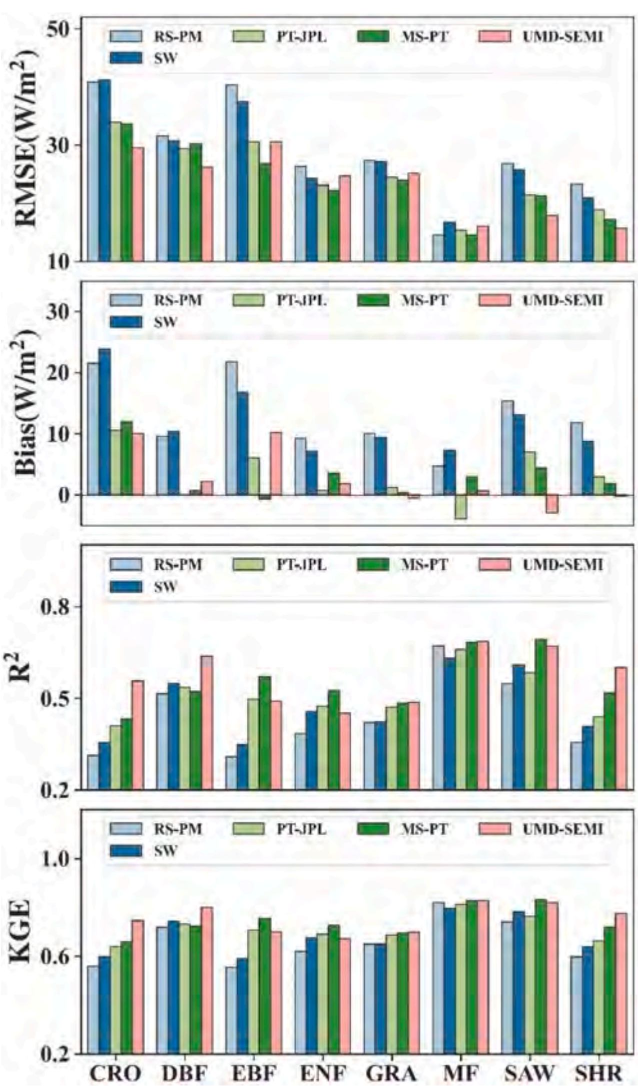

Fig. 7. Bar graphs of the statistics (KGE, R^2, bias and RMSE) of the comparisons between the 16-day LE from five physical LE algorithms and ground-measured data at 190 EC flux tower sites for different land cover types.

4.2. Integration of the five landsat-derived physical LE algorithms

Considering that none of the LE algorithms can provide a consistently best LE estimation across all land cover types, we used the CNN-LSTM algorithm along with the MLR, RF and DNN algorithms to improve the LE estimations by integrating five Landsat-derived physical LE algorithms, topography-related variables (elevation, aspect and slope) and EC observations. Fig. 9 shows the performances of the CNN-LSTM, MLR, RF and DNN integration algorithms when using the 10-fold cross-validation method for all 190 flux tower sites among different land cover types. It is notable that the estimated LE using the CNN-LSTM algorithm for different land cover types have higher KGE and R^2 and lower RMSE values compared to the MLR, RF and DNN integration algorithms. For the GRA flux tower sites, the CNN-LSTM algorithm provides better values of KGE of 0.76 and R^2 of 0.57 ($p < 0.01$) and a smaller RMSE of 22.1 W/m^2 than the other integration algorithms, although it has the worst performance compared to the other land cover types. For the ENF flux tower sites, the CNN-LSTM algorithm also exhibits the best capability among all of the integration algorithms, with the highest KGE of 0.77 and R^2 of 0.59 ($p < 0.01$) and the smallest RMSE of 20.9 W/m^2. The CNN-LSTM algorithm produces higher KGE (0.86) and R^2 (0.75, $p < 0.01$) values with an RMSE of 21.5 W/m^2 than the other integration algorithms for the CRO flux tower sites, and it exhibits better performance than the other land types. Similarly, the CNN-LSTM algorithm also performs better than the other integration algorithms for the MF flux tower sites, with an R^2 of 0.74 ($p < 0.01$) and RMSE of 15.1 W/m^2.

The overall performances of the CNN-LSTM, MLR, RF and DNN integration algorithms using the 10-fold cross-validation method are demonstrated in Fig. 10 for all 190 flux tower sites among all land cover types. It is clear that the estimated LE using all four integration algorithms are exhibit better performance than those of the individual Landsat-derived LE products. The integration algorithms provide reliable LE estimations with KGE values ranging from 0.76 to 0.81, R^2 values ranging from 0.58 to 0.66 ($p < 0.01$) and RMSE values ranging from 21.5 W/m^2 to 23.3 W/m^2. The best performance for LE estimation is provided by the CNN-LSTM algorithm with the highest KGE and R^2 values and the smallest RMSE value and is followed by the DNN, RF and MLR algorithms. Compared with the DNN algorithm, with the second-highest performance for LE estimations, the KGE yielded by the CNN-LSTM algorithm increased by approximately 0.04, R^2 increased by 0.06 ($p < 0.01$) and the RMSE decreased by approximately 1.6. Fig. 11 shows that the error histograms of the MLR, DNN and RF algorithms are biased toward large compared to ground-measured LE, whereas the CNN-LSTM algorithm biases are closer to zero, which indicates that the CNN-LSTM algorithm achieves the best LE estimates because it considers the influences of neighboring pixels and temporal dependency of the LE. In contrast, the MLR algorithm exhibits the worst performance, which demonstrates that linear combinations may not accurately simulate the

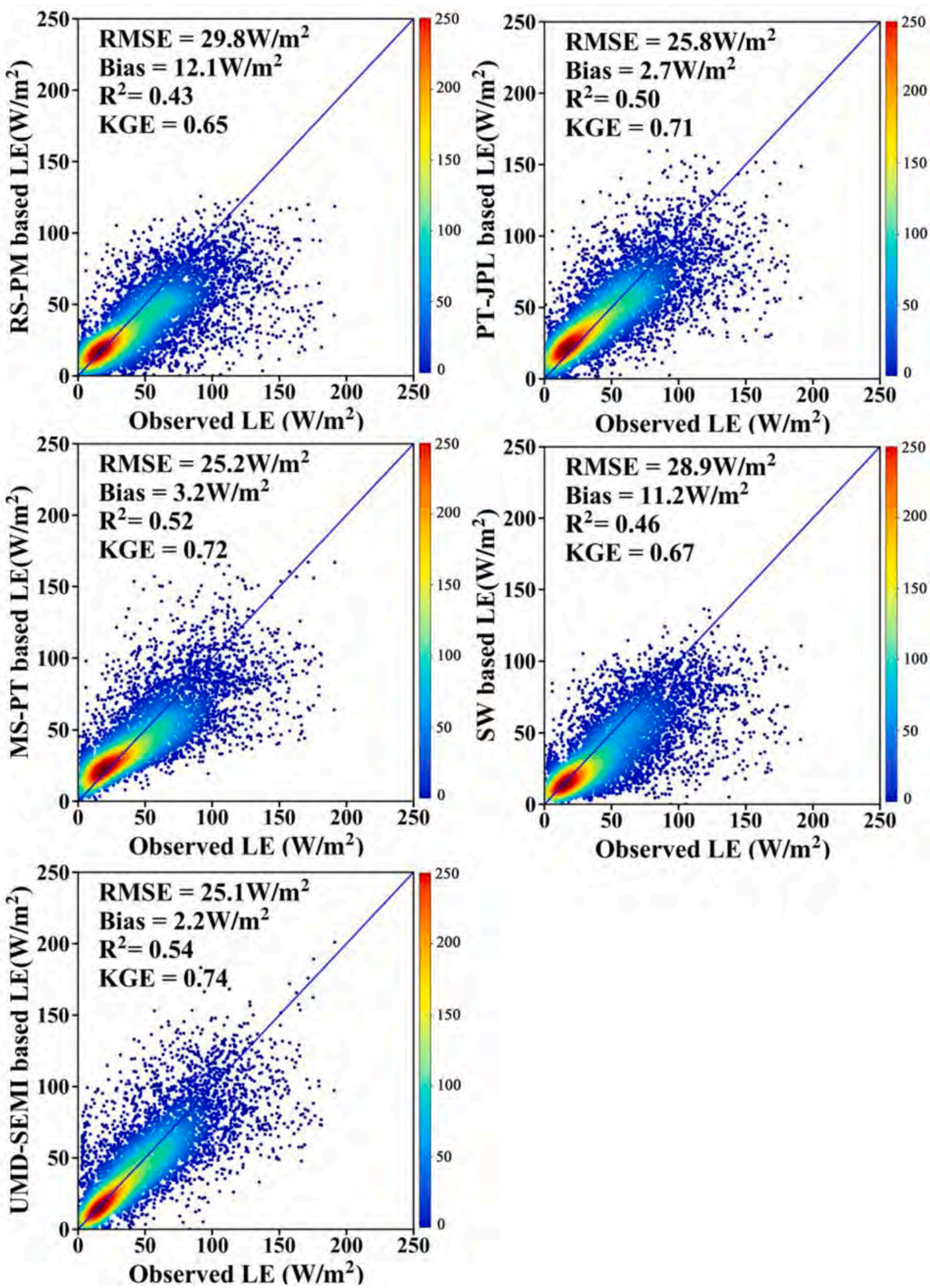

Fig. 8. Density scatter plots of the ground-measured LE and 16-day estimated LE from five physical LE algorithms at all 190 flux tower sites.

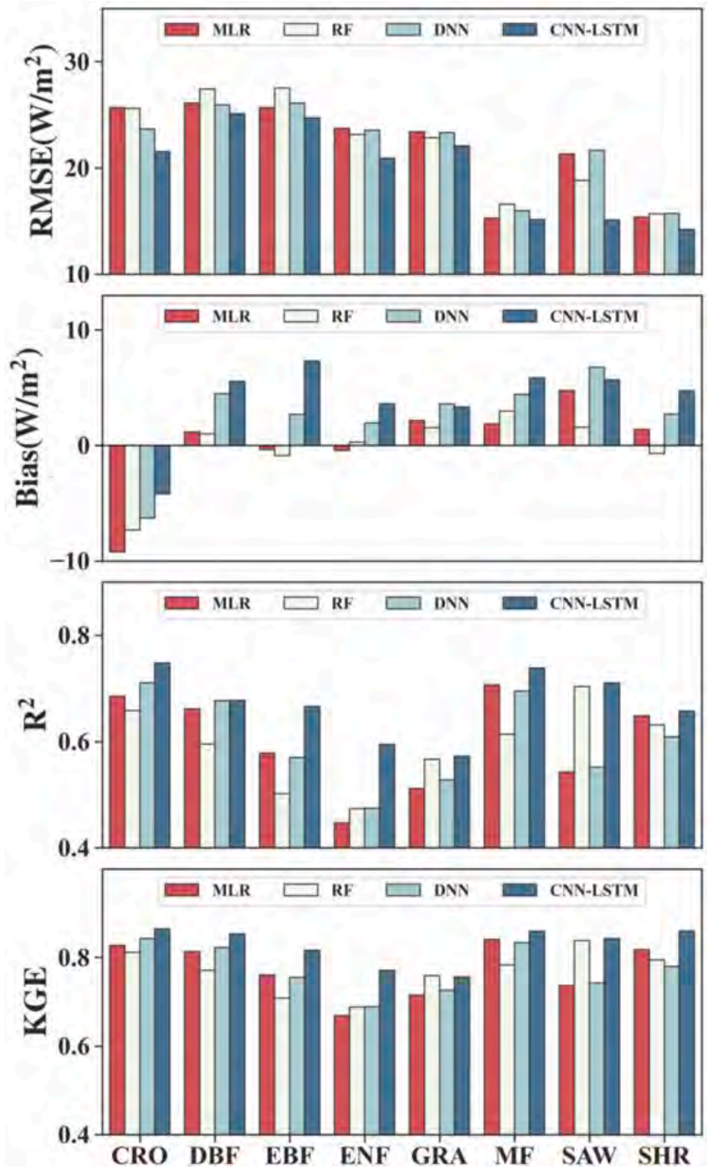

Fig. 9. Bar graphs of the statistics (KGE, R^2, bias and RMSE) of the comparison between the 16-day LE estimates using four integration algorithms and the ground-observed LE using the 10-fold cross-validation method at 190 EC flux tower sites for the different land cover types.

complex relationships among the ground-measured LE and input variables. The RF algorithm has better performance than the MLR because the RF, as an ensemble algorithm of machine learning, is a nonlinear model that fits complex relationships by using multiple decision trees to improve LE estimations. Similarly, the DNN algorithm has a more advanced nonlinear model structure and exhibits better performance than the MLR and RF integration algorithms.

Fig. 12 shows a time series of the 16-day EC observations and estimated LE from CNN-LSTM integration algorithm along with the physical LE algorithms for eight typical land cover types. Seasonal variation in LE is highly correlated with land cover types and phenological change due to the changes in vegetation and meteorological variables. The integrated LE estimates for cropland show multiple peaks, which may be caused by frequently agricultural irrigation activities. Compared with the individual Landsat-derived physical LE algorithms, the estimated LE obtained by using the CNN-LSTM integration algorithm provide obviously seasonal LE curves that are closest to the EC observations. Overall, the errors in the individual Landsat-derived physical LE algorithms product are approximately 26–35 %, and the errors in estimated LE based on the CNN-LSTM algorithm in this study are less than 20 %. Therefore, the CNN-LSTM integration algorithm can be applied to estimate Landsat-like LE with high accuracies at the global scale.

4.3. Case studies of mapping terrestrial LE

4.3.1. Agricultural field LE mapping

We chose an example of a 54×54 km agricultural field area (39.15°N - 39.64°N and 116.35°E - 116.83°E) in China on August 23, 2018, from Landsat data to estimate the 16-day LE using the CNN-LSTM integration algorithm (Fig. 13). The agricultural field area has high vegetation cover in most areas. In the northeastern part of this example area, the vegetation cover is relatively low. Fig. 13 shows the spatial LE patterns obtained from different LE products and from the CNN-LSTM integration algorithm along with the histograms of the frequency distribution of the LE values and the frequency distributions of the differences between each LE product and the CNN-LSTM algorithm results. The estimated LE have shown spatial variations across whole images, which are consistent with the large spatial changes in vegetation cover. This may be attributed to the fact that high vegetation transpiration occurs in agricultural field areas.

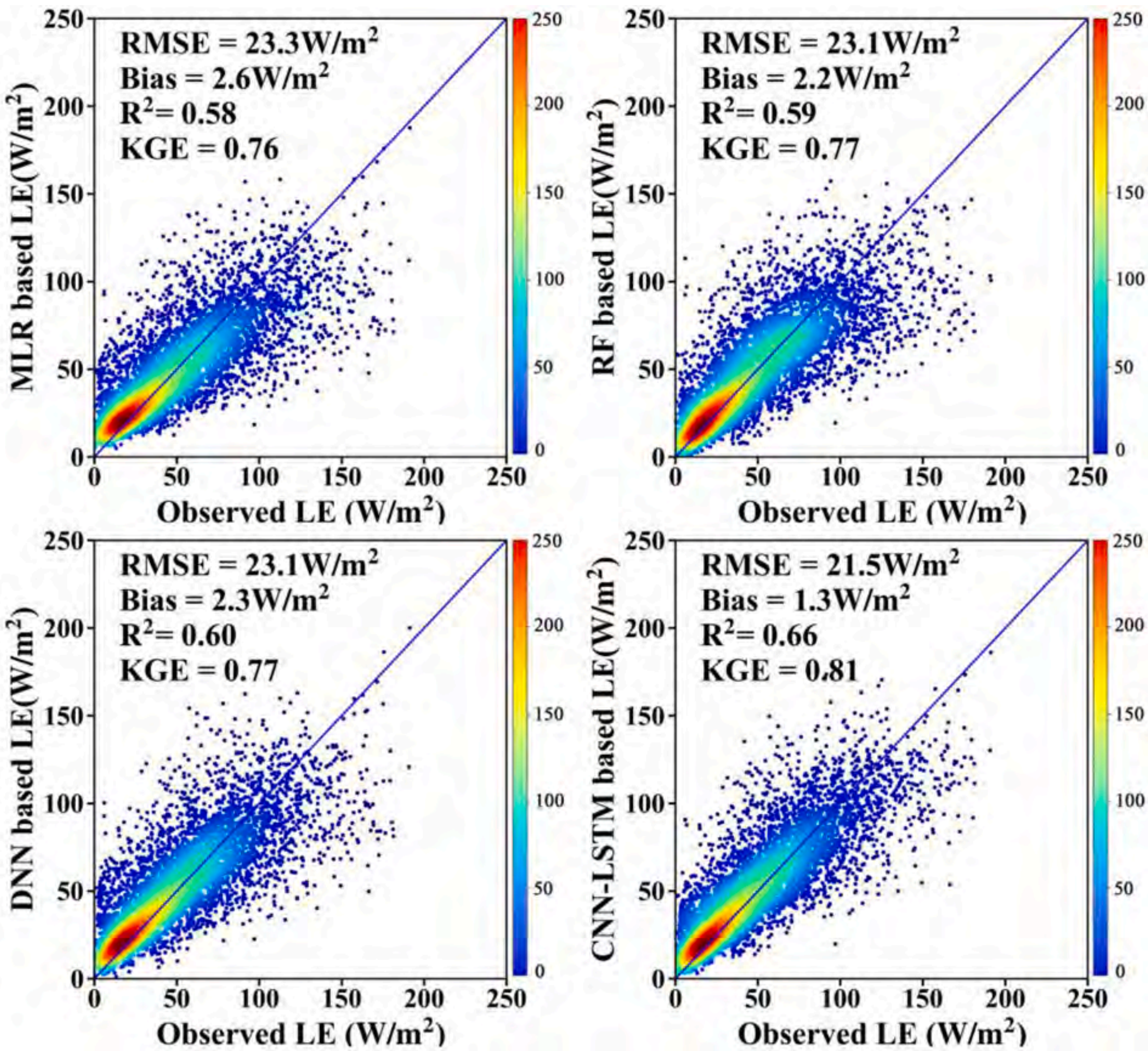

Fig. 10. Density scatter plots of the ground-measured LE and 16-day estimated LE from four integration algorithms using the 10-fold cross-validation method for all 190 EC flux tower sites. .

There are large differences among the estimated LE when using the CNN-LSTM integration algorithm and the five Landsat-derived physical LE algorithms. Generally, the CNN-LSTM algorithm exhibits intermediate LE values with a frequency histogram that is mainly concentrated at approximately 120 W/m^2, which is lower than those of the PT-JPL and RS-PM algorithms but is higher than those of the MS-PT, SW and UMD-SEMI algorithms. In contrast, the PT-JPL algorithm generates high LE estimates, and the LE values spans a full range from 110 to 132 W/m^2. The SW algorithm generates low LE values, and LE values spans a full range from 75 to 116 W/m^2. The UMD-SEMI algorithm and CNN-LSTM algorithm have the most similar spatial patterns and magnitudes of their values because the UMD-SEMI algorithm has the highest accuracy and more influence on the CNN-LSTM integration algorithm for LE estimates. The discrepancies in the LE estimates mainly stem from the different physics principles that are used by the different LE algorithms. For instance, the different parameterizations of the aerodynamic and surface resistances for both the RS-PM and SW algorithms will affect the accuracy of LE estimates (Mu et al., 2011; Shuttleworth and Wallace 1985).

4.3.2. Global terrestrial LE mapping

We applied the CNN-LSTM integration algorithm by integrating five physical LE algorithms, topography-related variables (elevation, aspect and slope) and EC observations to produce 16-day Landsat-like global terrestrial LE product (except for Antarctica) at 30-m spatial resolution for the 2013–2015 period. Fig. 14 shows the multiyear (2013–2015) average annual LE, and the estimated LE exhibit large regional variations and latitudinal gradients based on global climate patterns. The highest annual LE occurs in the tropical rainforests of South America, Central Africa, and Southeast Asia, while the lowest annual LE occurs in the Arctic and desert regions (*e.g.,* Sahara Desert) due to SM limitations and short growth seasons. Intermediate annual LE occurs in boreal and temperate forests. However, the global LE maps have stripping phenomenon due to the different Landsat images mosaic. The global terrestrial average annual LE is 36.4 W/m^2, which falls within the range of 34.1–42.7 W/m^2 that was inferred from 17 global terrestrial LE products (Wang and Dickinson, 2012).

The average seasonal LE patterns from 2013 to 2015 obtained using the CNN-LSTM integration algorithm exhibit distinct global seasonality (Fig. 15). The tropical rainforest regions maintain high LE values throughout the year, while savanna and tropical sparse forest regions have alternating dry and wet seasons. Strong seasonal LE variations occur in the high northern latitudes, where the LE has large variations with increases in summer and decreases in winter.

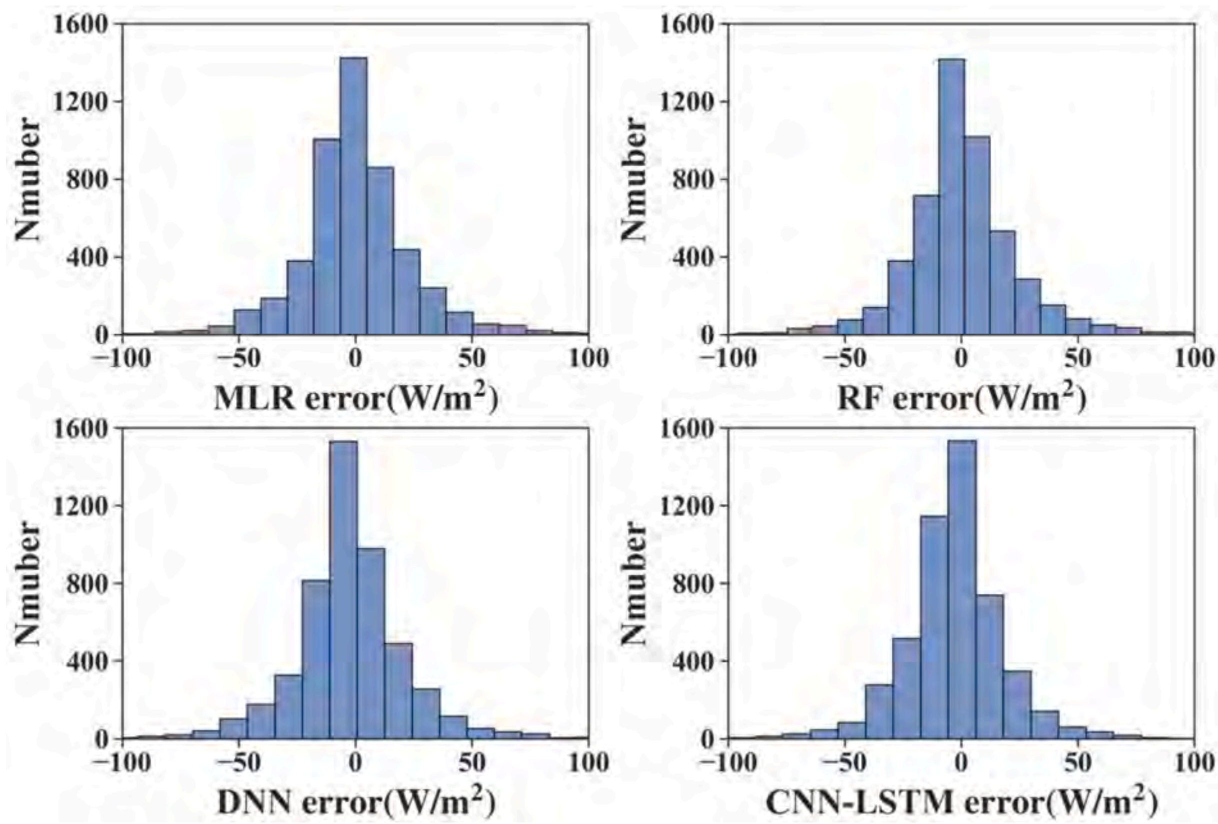

Fig. 11. Error histograms for the LE estimates from four integration algorithms for all 190 flux tower sites.

5. Discussion

5.1. Performance of the CNN-LSTM-ILE framework

5.1.1. Capability of the CNN-LSTM algorithm for LE estimations

The validation results for 190 EC flux towers demonstrated that the CNN-LSTM integration algorithm, when used for estimating LE is accurate and can yield a reliable 16-day LE product at 30-m spatial resolution. These results also show that the accuracy of the estimated LE when using the CNN-LSTM algorithm is significantly improved when compared with single-physical LE algorithms and other integration algorithms (MLR, RF and DNN). However, the CNN-LSTM algorithm shows the large inter-biome differences, performs better for the CRO, MF, DBF and SAW flux tower sites but performs worse for the EBF and ENF flux tower sites. For instance, the CNN-LSTM algorithm can account for more than 70 % of the LE variability for the CRO and DBF flux tower sites. Many satellite-based LE algorithms accurately simulate the LE via the NDVI or LAI, which accurately characterize the strong seasonality of vegetation variations (Yao et al., 2015; Yebra et al., 2013). Thus, the CNN-LSTM algorithm for integrating five vegetation-based LE algorithms improves the LE estimations. In contrast, the CNN-LSTM algorithm along with five Landsat-derived physical LE algorithms provides poor LE estimates for the ENF sites (average KGE of 0.77 and average RMSE of 20.9 W/m^2 for the CNN-LSTM algorithm). This may be attributed to the fact that the seasonal variations are weak in the ENF, where the saturation of NDVI to acquire the LE variations in this land cover type is limited (Huete et al., 2002; Yebra et al., 2013).

Our study found that the using CNN-LSTM integration algorithm for LE estimates provides not only superior results to the MLR, RF and DNN algorithms but also performs better than the CNN algorithm or LSTM algorithm alone (Table 2). The overall KGE of the 16-day LE estimations obtained from the CNN-LSTM algorithm is approximately 4–6 % higher than those of the above five integration methods. In the process of integrating the LE products, the CNN-LSTM algorithm makes the best use of the spatial and temporal information of the forcing inputs (Masolele et al., 2021; Wu et al., 2020). For an LE window of Landsat images, the surrounding pixel values affect the inner pixel values due to the horizontal transfer of energy and water between adjacent areas (Widlowski et al., 2006). Thus, the CNN window partially captures this spatial information of LE variability. Additionally, the LSTM has loops and allow the information of LE variability to persist to deal with time series LE data. Thus, the LSTM improves the accuracy of LE estimates from daily to 16-day values. By combining CNN with LSTM, the CNN-LSTM algorithm performs best for LE estimates among all of the integration algorithms used in this study. In contrast, although other machine learning integration algorithms also decrease the uncertainties in LE estimates by adjusting the linear or nonlinear weights of each LE product, the ability of these machine learning algorithms to estimate LE is limited because they do not fully consider the spatial and time series information contained in the samples (Bai et al., 2021; Bhattarai et al., 2016; Wagle et al., 2017).

5.1.2. Effects of the CNN-LSTM window size on LE estimations

To investigate the effects of the model window size on the LE estimations, we used different window sizes to train the CNN-LSTM integration algorithm. Fig. 16 shows that as the window size of the CNN-LSTM algorithm increases, the performance of the CNN-LSTM algorithm improves significantly. When the window size of the CNN-LSTM algorithm reaches 11 pixels, the CNN-LSTM algorithm provides the best performance with the largest R^2 of 0.66 ($p < 0.01$), largest KGE of 0.81 and smallest RMSE of 21.5 W/m^2. Window sizes larger than 11×11 pixels would lead to large errors in LE estimations when using the CNN-LSTM algorithm. This may be caused by the spatial mismatches between the footprints of the EC flux towers and the pixels of the Landsat-derived LE estimates (Baldocchi, 2008; Rienecker et al., 2011; Yao et al., 2017a). The footprints of the EC flux towers are approximately varying from tens

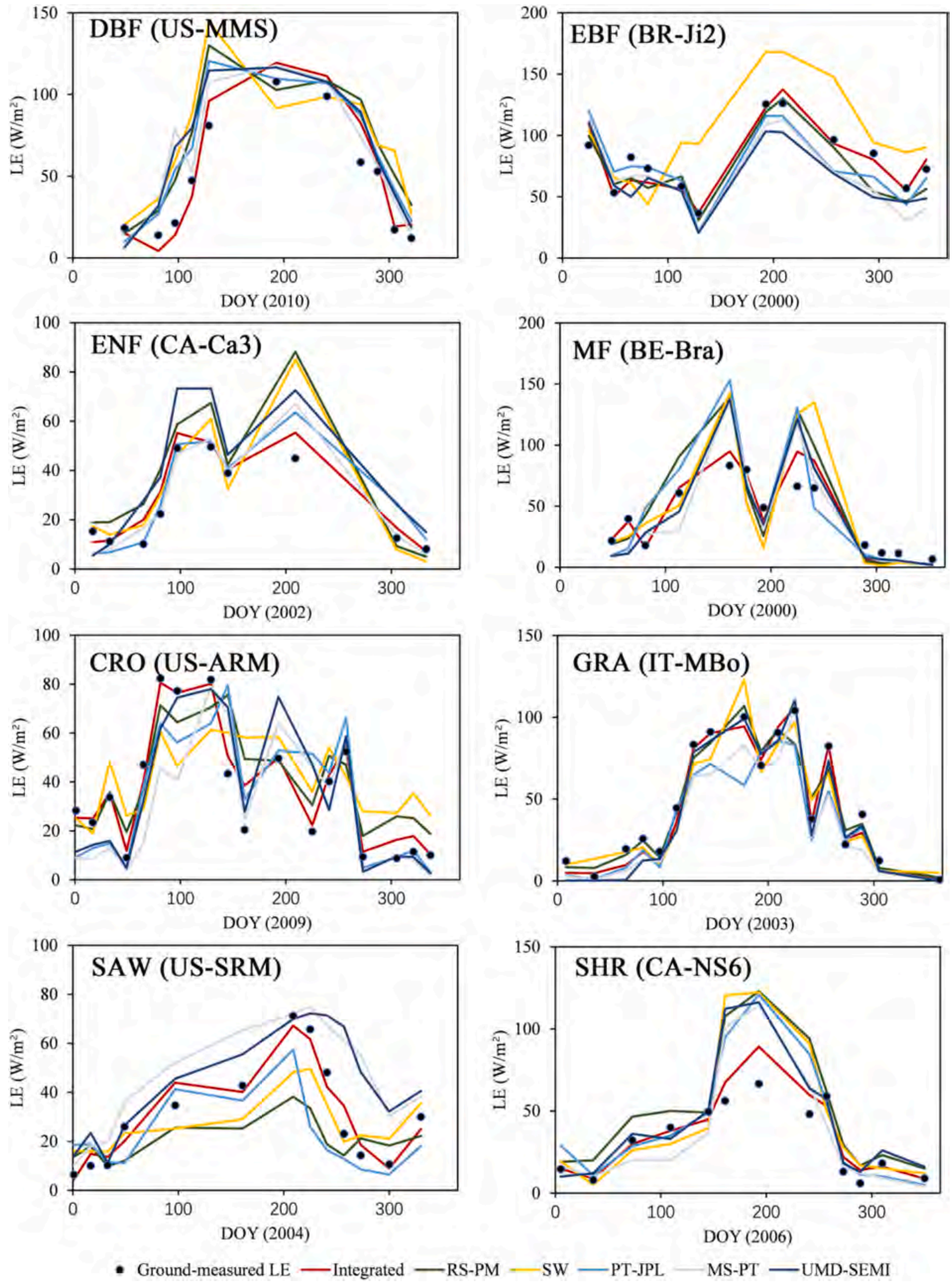

Fig. 12. Time series example of 16-day LE as ground-measured and estimated using physical LE algorithms (including CNN-LSTM integration algorithm) at eight validation sites.

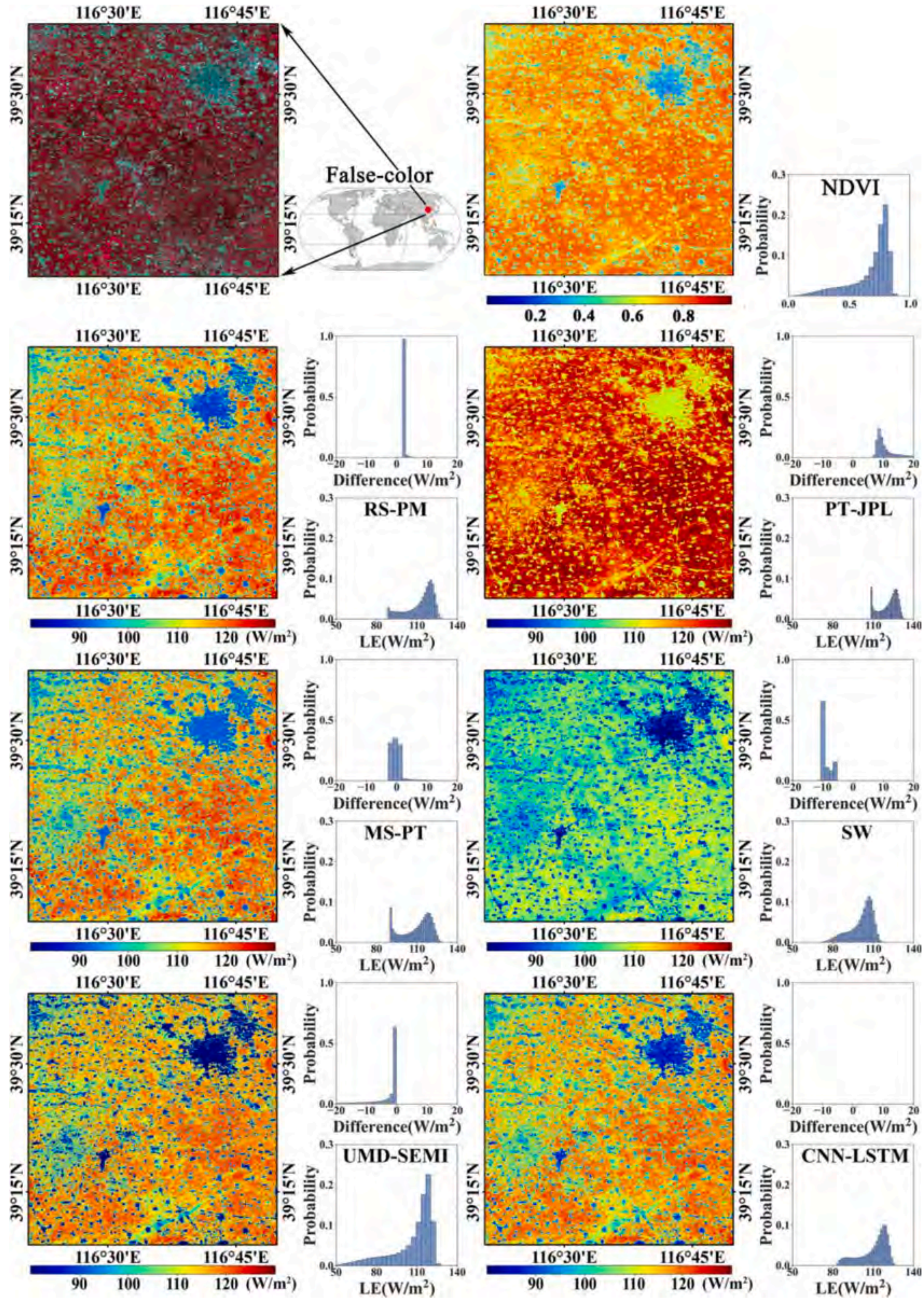

Fig. 13. Example of agricultural field area of a Landsat image with a false-color composite and NDVI on August 23, 2018, along with the 16-day LE spatial patterns of five LE algorithms and the CNN-LSTM integration algorithm results with the frequency histograms of the LE mappings and the differences among the LE products with the CNN-LSTM integration algorithm results.

of meters to several hundred meters for different land cover types, while the spatial resolution of the Landsat-derived LE estimates is approximately 30 m. The use of a suitable window size (330×330 m) in the CNN-LSTM algorithm can effectively characterize the footprints of the EC flux towers to improve LE estimations.

Fig. 17 presents an example of the EC flux tower footprints that were calculated using a Eulerian analytic flux footprint model (Kormann and Meixner 2001) of the flux source areas of the Daxing EC site (116.25° E, 39.53° N) on different dates. It is clear that the weight value contributed by the center pixel that corresponds to location of the EC flux tower is the largest, and the weight values are smaller toward the outside. Although the spatial distributions of the EC flux tower footprints vary

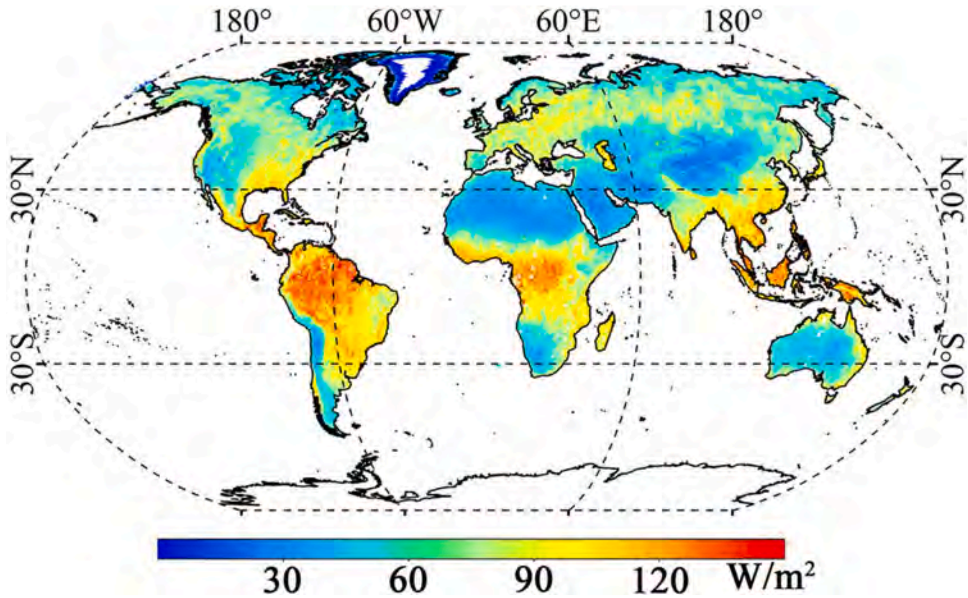

Fig. 14. Maps of the annual global terrestrial LE averaged for 2013–2015 at spatial resolution of 30-m that were obtained from the CNN-LSTM integration algorithm.

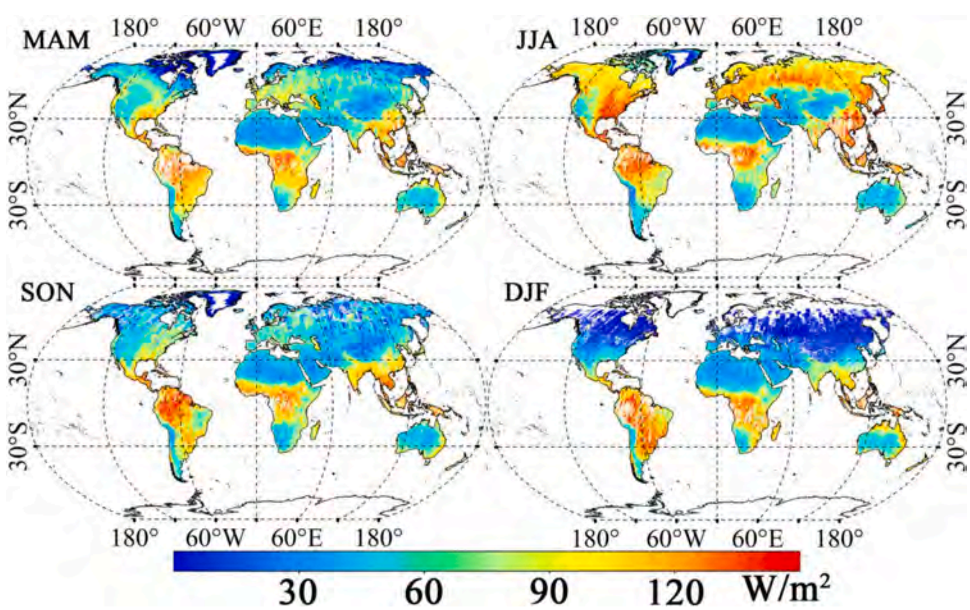

Fig. 15. The seasonality of the global terrestrial LE averaged for 2013–2015 at spatial resolution of 30-m that were obtained from the CNN-LSTM integration algorithm.

Table 2
Comparison of the LSTM, CNN and CNN-LSTM integration algorithms.

Algorithm	RMSE (W/m^2)	R^2	KGE
LSTM	23.2	0.59	0.74
CNN	22.9	0.60	0.75
CNN-LSTM	21.5	0.66	0.81

greatly for different dates (caused by wind direction and speed) (Baldocchi, 2008; Jia et al., 2012; Liu et al., 2016), the main contribution from the footprints of these flux tower sites to the LE values is confined to approximately 330 m, and a 11×11 (330×330 m) window size contains the pixels with the main weights for driving the CNN to obtain more valuable information for improving LE estimations. In contrast, if the window size is greater than 330×330 m, the more redundant information in the forcing data will lead to large errors in LE estimations. Meanwhile, the LSTM uses time series of the forcing data to extract the temporal dependency of this information to characterize the LE variations in the EC footprints. Therefore, the CNN-LSTM algorithm can utilize the space and time information of the LE products and topography-related variables to improve LE estimations.

5.1.3. Importance of input variables to LE estimations

Analyzing the importance of the forcing variables (RS-PM, SW, PT-JPL, MS-PT, UMD-SEMI, elevation, aspect and slope) to integrate the LE is crucial for understanding the impacts of these variables on the performance of the CNN-LSTM integration algorithm (Masolele et al., 2021). To evaluate the contribution of each variable to the CNN-LSTM algorithm, we removed one of the individual forcing variables in the CNN-LSTM algorithm and replicated the cross-validation process for testing algorithm performance. If a forcing variable was removed and

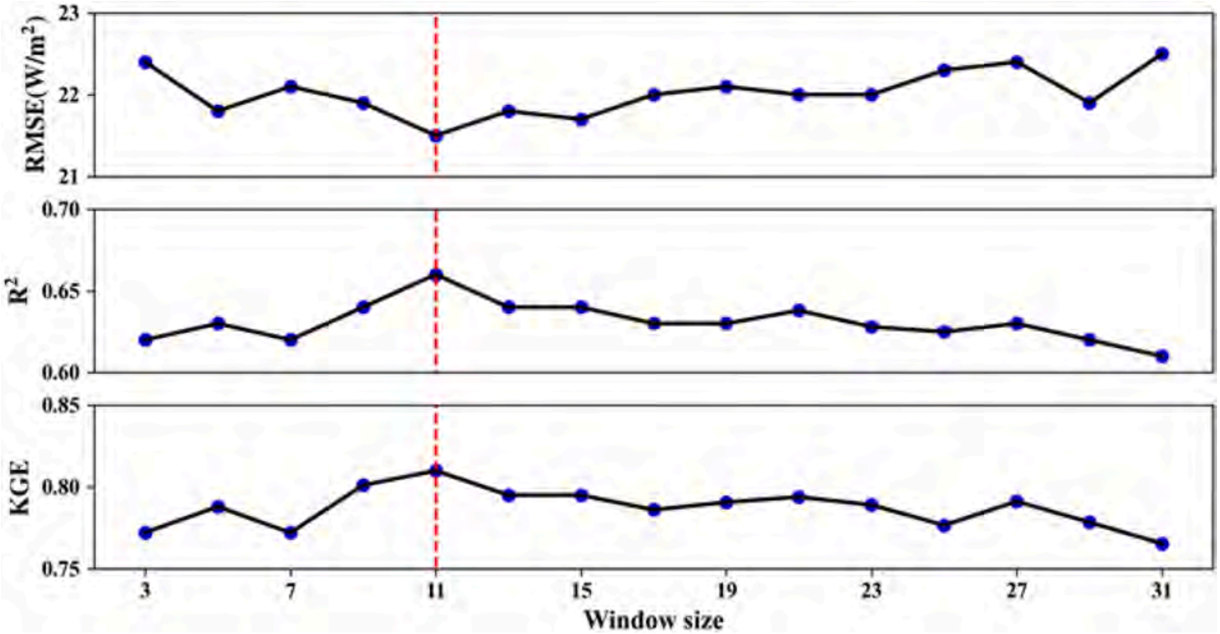

Fig. 16. Variations in RMSE, R^2 and KGE values of the estimated 16-day LE obtained from the CNN-LSTM algorithm with different window sizes (unit: pixel) at 190 EC sites.

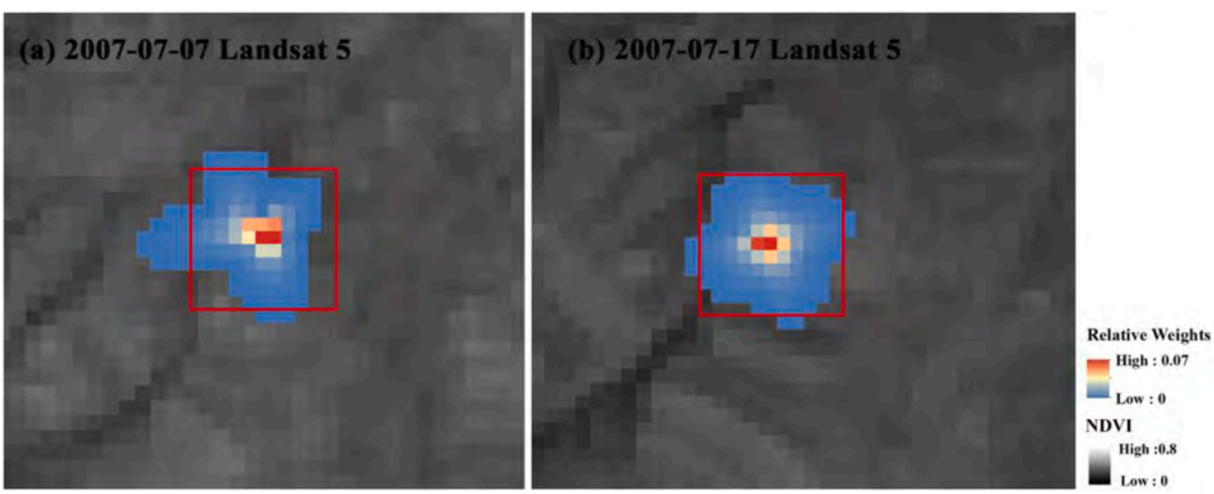

Fig. 17. Footprints of the Daxing EC flux tower site on different dates. The pixel values represent the contribution weights of the pixels to the EC flux tower observations. The red box indicates the 11×11 (330×330 m) window size of the Landsat images.

the larger the value of the decreased KGE was, the more important that variable was to the estimated LE.

The UMD-SEMI LE estimate is the most critical variable (KGE decreased by approximately 7 % when it is removed) due to its higher accuracy relative to the other four LE estimates (Fig. 18), which was calculated based on the Penman equation with empirically calibrated coefficients from 64 global EC sites (Wang et al., 2010). As PT algorithm-based LE estimates (Fisher et al., 2008; Yao et al., 2013), both the MS-PT and PT-JPL LE estimates also had relatively high importance (KGE decreased by approximately 5 % and 3 % when they are removed, respectively, due to their abilities to partition the total LE using by eco-physiological constraints (Ershadi et al., 2014; Talsma et al., 2018a, b; Wang and Dickinson, 2012). Additionally, both the SW and RS-PM LE estimates are also the key variables that directly lead to changes in the LE simulation (KGE decreased by approximately 4 % and 3 % if they are removed, respectively), which helps to improve the integrated LE.

Topography-related elevation, slope and aspect are also identified as valuable variables with respect to LE variations due to their effects on the redistribution of surface energy (Wei et al., 2017). When the elevation, slope and aspect were removed, the KGE decreased by 2 %, 1 % and 1 %, respectively (Fig 18). Increased elevation will result in a decrease in air temperature, which causes the LE to decrease significantly as the elevation increases (Goulden et al., 2012). In addition, both the aspect and slope will alter the received solar radiation, which in turn affects LE estimations due to the energy exchange between the earth and atmosphere (Allen et al., 2011; Cascone et al., 2019).

5.1.3.1. Generalization of the integration and upscaling LE estimations. Previous studies have focused on upscaling the LE values from EC flux tower sites to regional scales by using machine learning algorithms driven by satellite and meteorological variables as direct inputs (Jung et al., 2011; Wang and Dickinson 2012; Yamaç and Todorovic 2020). However, our study highlighted the integration of multiple Landsat-derived physical LE algorithms and topography-related

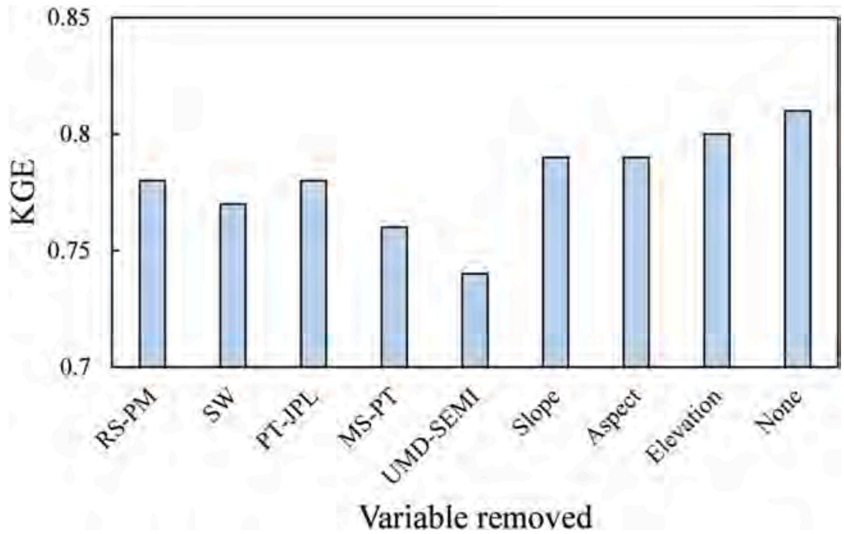

Fig. 18. Algorithm performance when removing different variables.

variables by using the CNN-LSTM integration algorithm. To compare the generalization differences between the integration of LE and upscaling of LE, we used the CNN-LSTM algorithm to implement the upscaling of LE that was directly driven by all of the forcing data of the five Landsat-derived physical LE models and topography data and then validated the upscaled LE estimates based on a 10-fold cross-validation. Fig. 19 shows that with the same satellite, meteorological variables, topography-related variables and EC observations, the upscaled LE estimates showed comparable performance with the integration of LE estimates (KGE of 0.79 and 0.81 for the upscaling and integrated LE, respectively).

Although the overall performances of the above two strategies are relatively similar, substantial discrepancies appear in areas where the vegetation is particularly sparse or dense. For the extreme cases of NDVI<0.20 or NDVI>0.80, the accuracies of the LE estimates that are obtained by integrating five Landsat-derived physical LE algorithms are systematically higher than those obtained by upscaling the LE from the flux tower sites to regional scales. This may be partially explained by the fact that the five Landsat-derived LE estimates used in the CNN-LSTM-ILE framework would be constrained by physical process-based LE algorithms that generalize more effectively under extreme cases (Shang et al. 2021; Zhao et al., 2019). For example, the MS-PT LE estimate that was used in the CNN-LSTM-ILE framework was generated by the physical process-based PT algorithm and outperformed the upscaled LE without physical constraints (KGE of 0.46 or 0.78) when NDVI<0.20 or NDVI>0.80. The upscaling strategy relies on the training samples, and the estimated LE under extreme cases may contain large errors (Chen et al., 2014; Shirmard et al., 2022). Therefore, our CNN-LSTM algorithm improves the generalization of the integration algorithms for extreme cases by coupling deep learning algorithms with model physics to maintain the extrapolation capacity that is inherited from the original Landsat-derived LE estimates.

5.2. *Uncertainties in LE estimations*

Although the proposed CNN-LSTM-ILE framework can improve LE estimations by capturing the spatial and temporal information related to the LE, the biases of the EC observations, errors in the individual physical LE algorithms, spatial mismatches between the source areas of the EC towers and Landsat pixels, and the CNN-LSTM integration algorithm itself could introduce uncertainties into LE estimations. The EC technique is currently considered the to be most accurate LE method that uses ground observations, but it still contains errors of approximately 5 %~20 % (Foken 2008; Twine et al., 2000). The filling of LE gaps from half-hour intervals to daily and 16-day periods is required to eliminate some invalid values, which will also introduce errors at levels

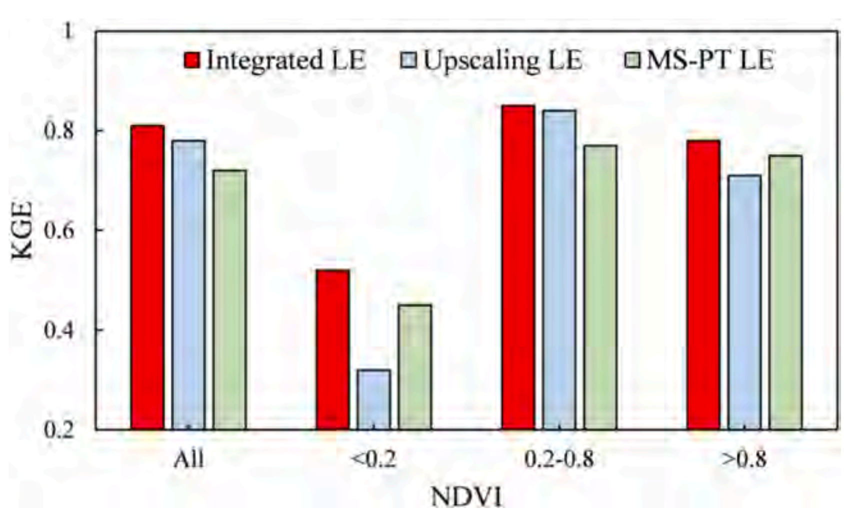

Fig. 19. Comparison of KGE of the MS-PT LE, upscaling LE and integrated LE estimates by using the CNN-LSTM algorithm for different NDVI cases.

of 5 % (Yao et al., 2021). Moreover, EC observations are affected by an energy imbalance problem that may be caused by the fact that the EC technique only acquires small eddies and ignores the large eddies present in the lower boundary layer, and the average energy closure ratio is approximately 0.80 for the global FLUXNET EC observations (Wilson et al., 2002). Although we have used the methods proposed by Twine et al. (2000) to correct the observed LE, there are still errors of 5–10 % (Mahrt 2010; Twine et al., 2000).

The errors in the individual Landsat-derived physical LE algorithms would also lead to uncertainties in the estimated LE when using the CNN-LSTM integration algorithm. The individual physical LE estimates are generated from the meteorological variables from the MERRA-2 datasets and vegetation structure variables (*e.g.,* LAI and FVC) obtained from Landsat data. Previous studies have indicated that there are large biases for the meteorological variables in the MERRA-2 datasets when compared to ground observations (Gelaro et al., 2017; Rienecker et al., 2011). Recent studies have found that MERRA-2 tends to underestimate the R_n levels by 5–10 % compared to the ground-measured R_n values (Gelaro et al., 2017; Guo et al., 2020). Additionally, the spatial resolution of the MERRA-2 data is relatively coarse (0.5°×0.625°), which will also cause certain errors when these data are spatially resampled to Landsat-like scales. Meanwhile, large biases are also present in the LAI and FVC that are derived from Landsat NDVI data (Demarty et al., 2007; Kandasamy et al., 2013). Eklundh et al. (2003) reported that there are errors of approximately 20–50 % for the LAI retrieved from Landsat NDVI data. Thus, input errors of the MERRA-2 and Landsat data and error propagation through the calculations, including LAI retrieval, gridded resampling and different data integrations, all affect the uncertainties of the integrated LE product.

The selection of the optimal window size in the CNN-LSTM integration algorithm may have partially solved the mismatch between the estimated LE and EC ground observations. However, there is still a small nonoverlapping spatial region between the optimal window size (11×11 pixels) and the EC footprint. The spatial ranges of the footprints of different EC towers vary from 100 to 400 m depending on the wind direction and speed. Thus, using a fixed window size in the CNN-LSTM integration algorithm can capture only approximately 92 % weights of the source areas of most of the EC flux towers (Burchard-Levine et al., 2021; Oishi et al., 2008). This may compromise the spatial representativeness of the integrated LE and ground observations and thereby introduce errors of 7–10 % into the validation results (Yao et al., 2021). Although the CNN-LSTM algorithm is an effective method, some issues in the CNN-LSTM integration algorithm itself may affect the accuracy of the estimated LE. The CNN-LSTM algorithm requires a large amount of training data and a limited amount of labeled data may lead to inferior performance (Ren et al., 2017). In addition, the CNN-LSTM algorithm is complicated and requires many hyperparameters, and the performance of the CNN-LSTM algorithm depends strongly on careful tuning (Ham et al., 2019; Lecun et al., 1998).

5.3. Algorithm merits and limitations

Compared to other LE algorithms, the CNN-LSTM integration algorithm has two merits. First, it has inherited the partial physical mechanisms of the individual process-based LE models and retains the high performance of deep learning algorithms for LE estimations. Relative to the individual process-based LE models, the CNN-LSTM algorithm improved the accuracy of LE estimations because it calibrated the multiple physical process-based LE products by using EC observations (Yuan et al., 2020). Similarly, the CNN-LSTM integration algorithm improved the generalization of integration algorithms for LE estimations under extreme cases when compared to the upscaled LE when using pure deep learning algorithms (Shang et al., 2021). Second, compared with other integration algorithms (MLR, RF and DNN), the CNN-LSTM integration algorithm has taken advantage of the spatial and temporal information contained in the forcing variables to improve the LE estimates. The inputs of this algorithm include the 16-day LE values of both the central Landsat pixels and those of the surrounding pixels, as well as the corresponding values of the topography-related variables and EC observations. Thus, both the CNN and LSTM exhibit high performance for LE estimates by processing these spatial and time series input data, respectively (Boulila et al., 2021).

Like other integration algorithms, the CNN-LSTM integration algorithm has three distinct limitations. First, the CNN-LSTM algorithm is a deep learning method that relies on a sufficient number of training samples to improve the robustness of the algorithm (LeCun et al., 2015). When sampling the LE products, the topography-related variables and EC observations are not representative and the CNN-LSTM algorithm introduces substantial errors into LE extrapolations. Second, the CNN-LSTM algorithm requires relatively lengthy processing times (about 5.2 s for 100 samples) to train the algorithm. Moreover, for generating a Landsat-like LE images, the CNN-LSTM algorithm is 15 times slower than the DNN algorithm. Future research will focus on improving the deep learning algorithms by coupling with a physical-based LE model to generate high-spatial-resolution global terrestrial LE products. Third, our current study does not include temperature-based models like the Surface Temperature Initiated Closure (STIC) model (Bai et al., 2022; Mallick et al., 2015), which have shown potential in improving flux estimations in varied ecosystems. Future research could benefit from integrating such models, enhancing estimation accuracy, especially under extreme moisture conditions.

6. Conclusions

We developed a deep CNN-LSTM-based integrated LE (CNN-LSTM-ILE) framework by integrating five Landsat-derived physical LE algorithms (RS-PM, SW, PT-JPL, MS-PT, and UMD-SEMI LE algorithms), topography-related variables (elevation, slope and aspect) and EC ground observations to improve the global terrestrial Landsat-like LE. The five Landsat-derived physical LE algorithms driven by the MERRA-2 meteorological datasets and Landsat data were assessed using the EC ground observations at 190 global EC flux tower sites during 2000–2015. We found large discrepancies for the five Landsat-derived physical LE algorithms for LE estimation among the different land cover types.

A series of cross-validations demonstrates that the CNN-LSTM integration algorithm yields better performance for LE estimates with KGE ranging from 0.76 to 0.81, R^2 values ranging from 0.58 to 0.66 ($p < 0.01$) and RMSE ranging from 21.5 W/m^2 to 23.3 W/m^2, for different land cover types than the other machine learning integration algorithms (MLR, RF and DNN) and the individual physical LE algorithms. Compared with the upscaling of LE from site to regional scales, the CNN-LSTM algorithm that combines deep learning algorithm and physical process-based LE model has improved the generalization of integration algorithms for extreme cases.

The CNN-LSTM integration algorithm was also applied to estimate the global terrestrial Landsat-like LE by using five Landsat-derived physical LE algorithms, elevation, slope and aspect data. The annual mean global terrestrial Landsat-like LE during 2013–2015 that were estimated by the CNN-LSTM-ILE framework was approximately 36.4 W/m^2, which is consistent with the results of other studies. Our study has provided a valuable bridge between the finer scale (several decades meters) and large pixel scales of the coarse-resolution LE products (several kilometers). Future work will consist of decreasing the integration algorithm complexity and its dependence on training data and to produce a long-term series of global high-spatial-resolution LE products.

CRediT authorship contribution statement

Xiaozheng Guo: Conceptualization, Data curation, Formal analysis, Investigation, Methodology, Software, Validation, Visualization, Writing – original draft, Writing – review & editing. **Yunjun Yao:**

Conceptualization, Data curation, Formal analysis, Funding acquisition, Project administration, Resources, Supervision, Writing – review & editing. **Qingxin Tang:** Data curation, Writing – review & editing. **Shunlin Liang:** Writing – review & editing. **Changliang Shao:** Writing – review & editing. **Joshua B. Fisher:** Writing – review & editing. **Jiquan Chen:** Conceptualization, Writing – review & editing. **Kun Jia:** Writing – review & editing. **Xiaotong Zhang:** Data curation. **Ke Shang:** Data curation. **Junming Yang:** Data curation. **Ruiyang Yu:** Data curation. **Zijing Xie:** Data curation. **Lu Liu:** Data curation. **Jing Ning:** Data curation. **Lilin Zhang:** Data curation.

Declaration of competing interest

The authors declare that they have no known competing financial interests or personal relationships that could have appeared to influence the work reported in this paper.

Data availability

The authors do not have permission to share data.

Acknowledgments

This work was supported by the Natural Science Fund of China (No. 42171310 and No. 42192581) and the Special Foundation for National Science and Technology Basic Research Program of China (2019FY102000). Acknowledgement for the data support from "National Earth System Science Data Center, National Science & Technology Infrastructure of China (http://www.geodata.cn)". The authors would like to thank Prof. Tao He from School of Remote Sensing and Information Engineering, Wuhan University, China for providing Hi-GLASS data. This work used eddy covariance data acquired by the FLUXNET community and in particular by the following networks: AmeriFlux (U.S. Department of Energy, Biological and Environmental Research, Terrestrial Carbon Program (DE-FG02–04ER63917 and DE-FG02–04ER63911)), AfriFlux, AsiaFlux, CarboAfrica, CarboEuropeIP, CarboItaly, CarboMont,ChinaFlux, Fluxnet-Canada (supported by CFCAS, NSERC, BIOCAP, Environment Canada, and NRCan), GreenGrass, KoFlux, LBA, NECC, OzFlux, TCOS-Siberia, USCCC. We acknowledge the financial support to the eddy covariance data harmonization provided by CarboEuropeIP, FAO-GTOS-TCO, iLEAPS, Max Planck Institute for Biogeochemistry, National Science Foundation, University of Tuscia, Université Laval, Environment Canada and US Department of Energy and the database development and technical support from Berkeley Water Center, Lawrence Berkeley National Laboratory, Microsoft Research eScience, Oak Ridge National Laboratory, University of California –Berkeley and the University of Virginia. Other ground-measured data were obtained from the *GAME AAN* (http://aan.suiri.tsukuba.ac.jp/), the Coordinated Enhanced Observation Project (*CEOP*) in arid and semi-arid regions of northern China (http://observation.tea.ac.cn/), and the water experiments of Environmental and Ecological Science Data Center for West China (http:// westdc.westgis.ac.cn/water).

References

Allen, R., Pereira, L., Raes, D., Smith, M., Allen, R.G., Pereira, L.S., Martin, S., 1998. Crop evapotranspiration: guidelines for computing crop water requirements, FAO irrigation and drainage paper 56. FAO 56.
Allen, R.G., Pereira, L.S., Howell, T.A., Jensen, M.E., 2011. Evapotranspiration information reporting: I. Factors governing measurement accuracy. Agric. Water Manag. 98, 899–920.
Allen, R.G., Tasumi, M., Trezza, R., 2007. Satellite-based energy balance for mapping evapotranspiration with internalized calibration (METRIC) - model. J. Irrig. Drain. Eng. 133, 380–394.
Amazirh, A., Er-Raki, S., Chehbouni, A., Rivalland, V., Diarra, A., Khabba, S., Ezzahar, J., Merlin, O., 2017. Modified Penman–Monteith equation for monitoring evapotranspiration of wheat crop: relationship between the surface resistance and remotely sensed stress index. Biosyst. Eng. 164, 68–84.
Anderson, M.C., Norman, J.M., Diak, G.R., Kustas, W.P., Mecikalski, J.R., 1997. A two-source time-integrated model for estimating surface fluxes using thermal infrared remote sensing. Remote Sens. Environ. 60, 195–216.
Anderson, M.C., Norman, J.M., Kustas, W.P., Houborg, R., Starks, P.J., Agam, N., 2008. A thermal-based remote sensing technique for routine mapping of land-surface carbon, water and energy fluxes from field to regional scales. Remote Sens. Environ. 112, 4227–4241.
Anderson, M.C., Yang, Y., Xue, J., Knipper, K.R., Yang, Y., Gao, F., Hain, C.R., Kustas, W. P., Cawse-Nicholson, K., Hulley, G., Fisher, J.B., Alfieri, J.G., Meyers, T.P., Prueger, J., Baldocchi, D.D., Rey-Sanchez, C., 2021. Interoperability of ECOSTRESS and Landsat for mapping evapotranspiration time series at sub-field scales. Remote Sens. Environ. 252, 112189.
Bai, Y., Bhattarai, N., Mallick, K., Zhang, S., Hu, T., Zhang, J., 2022. Thermally derived evapotranspiration from the surface temperature initiated closure (STIC) model improves cropland GPP estimates under dry conditions. Remote Sens. Environ. 271, 112901.
Bai, Y., Zhang, S., Bhattarai, N., Mallick, K., Liu, Q., Tang, L.L., Im, J., Guo, L., Zhang, J. H., 2021. On the use of machine learning based ensemble approaches to improve evapotranspiration estimates from croplands across a wide environmental gradient. Agric. For. Meteorol. 298.
Baldocchi, D., 2008. Breathing of the terrestrial biosphere: lessons learned from a global network of carbon dioxide flux measurement systems. Aust. J. Bot. 56, 1–26.
Bastiaanssen, W.G.M., Menenti, M., Feddes, R.A., Holtslag, A.A.M., 1998a. A remote sensing surface energy balance algorithm for land (SEBAL) - 1. Formulation. J. Hydrol. 212, 198–212.
Bastiaanssen, W.G.M., Pelgrum, H., Wang, J., Ma, Y., Moreno, J.F., Roerink, G.J., van der Wal, T., 1998b. A remote sensing surface energy balance algorithm for land (SEBAL) - 2. Validation. J. Hydrol. 212, 213–229.
Bhattarai, N., Shaw, S.B., Quackenbush, L.J., Im, J., Niraula, R., 2016. Evaluating five remote sensing based single-source surface energy balance models for estimating daily evapotranspiration in a humid subtropical climate. Int. J. Appl. Earth Obs. Geoinf. 49, 75–86.
Boulila, W., Ghandorh, H., Khan, M.A., Ahmed, F., Ahmad, J., 2021. A novel CNN-LSTM-based approach to predict urban expansion. Ecol. Inform. 64, 101325.
Breiman, L., 2001. Random forests. Mach. Learn. 45, 5–32.
Burchard-Levine, V., Nieto, H., Riaño, D., Migliavacca, M., El-Madany, T.S., Guzinski, R., Carrara, A., Martín, M.P, 2021. The effect of pixel heterogeneity for remote sensing based retrievals of evapotranspiration in a semi-arid tree-grass ecosystem. Remote Sens. Environ. 260, 112440.
Cascone, S, Coma, J, Gagliano, A, Pérez, G, 2019. The evapotranspiration process in green roofs: a review. Build. Environ. 147, 337–355.
Chang, Y.P., Luo, B., 2019. Bidirectional convolutional LSTM neural network for remote sensing image super-resolution. Remote Sens. 11.
Liang, S., Feng, J., Fisher, J.B., Li, X., Li, X., Liu, S., Ma, Z., Miyata, A., Mu, Q., Sun, L., Tang, J., Wang, K., Wen, J., Xue, Y., Yu, G., Zha, T., Zhang, L., Zhang, Q., Zhao, T., Zhao, L., Yuan, W., 2014. Comparison of satellite-based evapotranspiration models over terrestrial ecosystems in China. Remote Sens. Environ. 140, 279–293.
Chen, Y., Yuan, W.P., Xia, J.Z., Fisher, J.B., Dong, W.J., Zhang, X.T., Liang, S.L., Ye, A.Z., Cai, W.W., Feng, J.M., 2015. Using Bayesian model averaging to estimate terrestrial evapotranspiration in China. J. Hydrol. 528, 537–549.
Demarty, J., Chevallier, F., Friend, A.D., Viovy, N., Piao, S.L., Ciais, P., 2007. Assimilation of global MODIS leaf area index retrievals within a terrestrial biosphere model. Geophys. Res. Lett. 34.
Eklundh, L., Hall, K., Eriksson, H., Ardo, J., Pilesjo, P., 2003. Investigating the use of landsat thematic mapper data for estimation of forest leaf area index in southern Sweden. Can. J. Remote Sens. 29, 349–362.
Elnashar, A., Wang, L., Wu, B., Zhu, W., Zeng, H., 2021. Synthesis of global actual evapotranspiration from 1982 to 2019. Earth Syst. Sci. Data 13 (2), 447–480.
Ershadi, A., Mccabe, M.F., Evans, J.P., Chaney, N.W., Wood, E.F., 2014. Multi-site evaluation of terrestrial evaporation models using FLUXNET data. Agric. For. Meteorol. 187, 46–61.
Esteva, A., Robicquet, A., Ramsundar, B., Kuleshov, V., DePristo, M., Chou, K., Cui, C., Corrado, G., Thrun, S., Dean, J., 2019. A guide to deep learning in healthcare. Nat. Med. 25, 24–29.
Fisher, J.B., DeBiase, T.A., Qi, Y., Xu, M., Goldstein, A.H., 2005. Evapotranspiration models compared on a Sierra Nevada forest ecosystem. Environ. Model. Softw. 20 (6), 783–796.
Fisher, J.B., Melton, F., Middleton, E., Hain, C., Anderson, M., Allen, R., McCabe, M.F., Hook, S., Baldocchi, D., Townsend, P.A., Kilic, A., Tu, K., Miralles, D.D., Perret, J., Lagouarde, J.P., Waliser, D., Purdy, A.J., French, A., Schimel, D., Famiglietti, J.S., Stephens, G., Wood, E.F., 2017. The future of evapotranspiration: global requirements for ecosystem functioning, carbon and climate feedbacks, agricultural management, and water resources. Water Resour. Res. 53, 2618–2626.
Fisher, J.B., Lee, B., Purdy, A.J., Halverson, G.H., Dohlen, M.B., Cawse-Nicholson, K., et al., 2020. ECOSTRESS: nASA's next generation mission to measure evapotranspiration from the international space station. Water Resour. Res. 56, e2019WR026058.
Feng, F., Li, X.L., Yao, Y.J., Liang, S.L., Chen, J.Q., Zhao, X., Jia, K., Pinter, K., McCaughey, J.H., 2016. An empirical orthogonal function-based algorithm for estimating terrestrial latent heat flux from eddy covariance, meteorological and satellite observations. PLoS One 11.
Fisher, J.B., Tu, K.P., Baldocchi, D.D., 2008. Global estimates of the land-atmosphere water flux based on monthly AVHRR and ISLSCP-II data, validated at 16 FLUXNET sites. Remote Sens. Environ. 112, 901–919.

Foken, T., 2008. The energy balance closure problem: an overview. Ecol. Appl. 18, 1351–1367.
Gelaro, R., McCarty, W., Suarez, M.J., Todling, R., Molod, A., Takacs, L., Randles, C.A., Darmenov, A., Bosilovich, M.G., Reichle, R., Wargan, K., Coy, L., Cullather, R., Draper, C., Akella, S., Buchard, V., Conaty, A., da Silva, A.M., Gu, W., Kim, G.K., Koster, R., Lucchesi, R., Merkova, D., Nielsen, J.E., Partyka, G., Pawson, S., Putman, W., Rienecker, M., Schubert, S.D., Sienkiewicz, M., Zhao, B., 2017. The modern-era retrospective analysis for research and applications, version 2 (MERRA-2). J. Clim. 30, 5419–5454.
Glenn, E.P., Doody, T.M., Guerschman, J.P., Huete, A.R., King, E.A., McVicar, T.R., Van Dijk, A.I.J.M., Van Niel, T.G., Yebra, M., Zhang, Y., 2011. Actual evapotranspiration estimation by ground and remote sensing methods: the Australian experience. Hydrol. Process. 25, 4103–4116.
Goulden, M.L., Anderson, R.G., Bales, R.C., Kelly, A.E., Meadows, M., Winston, G.C., 2012. Evapotranspiration along an elevation gradient in California's Sierra Nevada. J. Geophys. Res. Biogeosciences 117.
Graves, A., Schmidhuber, J., 2005. Framewise phoneme classification with bidirectional LSTM and other neural network architectures. Neural Networks 18, 602–610.
Guo, X.Z., Yao, Y.J., Zhang, Y.H., Lin, Y., Jiang, B., Jia, K., Zhang, X.T., Xie, X.H., Zhang, L.L., Shang, K., Yang, J.M., Bei, X.Y., 2020. Discrepancies in the simulated global terrestrial latent heat flux from GLASS and MERRA-2 surface net radiation products. Remote Sens. 12.
Guo, Y.M., Liu, Y., Oerlemans, A., Lao, S.Y., Wu, S., Lew, M.S., 2016. Deep learning for visual understanding: a review. Neurocomputing. 187, 27–48.
Gupta, H.V., Kling, H., Yilmaz, K.K., Martinez, G.F., 2009. Decomposition of the mean squared error and NSE performance criteria: implications for improving hydrological modelling. J. Hydrol. 377, 80–91.
Ham, Y..G., Kim, J..H., Luo, J..J., 2019. Deep learning for multi-year ENSO forecasts. Nature 573, 568–572.
Hochreiter, S, Schmidhuber, J, 1997. Long short-term memory. Neural Comput. 9, 1735–1780.
Hornik, K, 1991. Approximation capabilities of multilayer feedforward networks. Neural Netw. 4, 251–257.
Huete, A, Didan, K., Miura, T., Rodriguez, E.P., Gao, X., Ferreira, L.G., 2002. Overview of the radiometric and biophysical performance of the MODIS vegetation indices. Remote Sens. Environ. 83, 195–213.
Jia, Z.Z., Liu, S.M., Xu, Z.W., Chen, Y.J., Zhu, M.J., 2012. Validation of remotely sensed evapotranspiration over the Hai River Basin, China. J. Geophys. Res. Atmos. 117.
Jiang, B., Han, J., Liang, H., Liang, S., Yin, X., Peng, J., He, T., Ma, Y., 2023. The Hi-GLASS all-wave daily net radiation product: algorithm and product validation. Sci. Remote Sens. 23, 100080.
Jin, H., Li, A., Liang, S., Ma, H., Xie, X., Liu, T., He, T., 2022. Generating high spatial resolution GLASS FAPAR product from Landsat images. Sci. Remote Sens. 6, 100060.
Jin, H., Li, A., Xu, W., Xiao, Z., Jiang, J., Xue, H., 2019. Evaluation of topographic effects on multiscale leaf area index estimation using remotely sensed observations from multiple sensors. ISPRS J. Photogramm. Remote Sens. 154, 176–188.
Jung, M., Reichstein, M., Margolis, H.A., Cescatti, A., Richardson, A.D., Arain, M.A., Arneth, A., Bernhofer, C., Bonal, D., Chen, J., Gianelle, D., Gobron, N., Kiely, G., Kutsch, W., Lasslop, G., Law, B.E., Lindroth, A., Merbold, L., Montagnani, L., Moors, E.J., Papale, D., Sottocornola, M., Vaccari, F., Williams, C., 2011. Global patterns of land-atmosphere fluxes of carbon dioxide, latent heat, and sensible heat derived from eddy covariance, satellite, and meteorological observations. J. Geophys. Res. Biogeosciences 116.
Kalma, J.D., McVicar, T.R., McCabe, M.F., 2008. Estimating land surface evaporation: a review of methods using remotely sensed surface temperature data. Surv. Geophys. 29, 421–469.
Kandasamy, S., Baret, F., Verger, A., Neveux, P., Weiss, M., 2013. A comparison of methods for smoothing and gap filling time series of remote sensing observations - application to MODIS LAI products. Biogeosciences 10, 4055–4071.
Ke, Y, Im, J, Park, S, Gong, H, 2017. Spatiotemporal downscaling approaches for monitoring 8-day 30m actual evapotranspiration. ISPRS J. Photogramm. Remote Sens. 126, 79–93.
Kessomkiat, W., Franssen, H.J.H., Graf, A., Vereecken, H., 2013. Estimating random errors of eddy covariance data: an extended two-tower approach. Agric. For. Meteorol. 171, 203–219.
Khaldi, A., Khaldi, A., Hamimed, A, 2014. Using the priestley-taylor expression for estimating actual evapotranspiration from satellite landsat ETM + data. Proc. IAHS 364, 398–403.
Kool, D, Agam, N, Lazarovitch, N, Heitman, J.L, Sauer, T.J, Ben-Gal, A, 2014. A review of approaches for evapotranspiration partitioning. Agric. For. Meteorol. 184, 56–70.
Kormann, R., Meixner, F.X., 2001. An analytical footprint model for non-neutral stratification. Bound. Layer Meteorol. 99, 207–224.
Kraft, B., Jung, M., Körner, M., Koirala, S., Reichstein, M., 2021. Towards hybrid modeling of the global hydrological cycle. Hydrol. Earth Syst. Sci. 26, 1579–1614.
Kustas, W., Anderson, M., 2009. Advances in thermal infrared remote sensing for land surface modeling. Agric. For. Meteorol. 149, 2071–2081.
LeCun, Y., Bengio, Y., Hinton, G., 2015. Deep learning. Nature 521, 436–444.
Lecun, Y., Bottou, L., Bengio, Y., Haffner, P., 1998. Gradient-based learning applied to document recognition. Proc. IEEE 86, 2278–2324.
Li, Z.L., Tang, R.L., Wan, Z.M., Bi, Y.Y., Zhou, C.H., Tang, B.H., Yan, G.J., Zhang, X.Y., 2009. A review of current methodologies for regional evapotranspiration estimation from remotely sensed data. Sensors 9, 3801–3853.
Liang, S.L., Wang, K.C., Zhang, X.T., Wild, M., 2010. Review on estimation of land surface radiation and energy budgets from ground measurement, remote sensing and model simulations. IEEE J. Sel. Top. Appl. Earth Obs. Remote Sens. 3, 225–240.
Lin, S., Huang, X., Zheng, Y., Zhang, X., Yuan, W., 2022. An open data approach for estimating vegetation gross primary production at fine spatial resolution. Remote Sens. 14, 2651.
Liu, S.M., Xu, Z.W., Song, L.S., Zhao, Q.Y., Ge, Y., Xu, T.R., Ma, Y.F., Zhu, Z.L., Jia, Z.Z., Zhang, F., 2016. Upscaling evapotranspiration measurements from multi-site to the satellite pixel scale over heterogeneous land surfaces. Agric. For. Meteorol. 230, 97–113.
Mahrt, L, 2010. Computing turbulent fluxes near the surface: needed improvements. Agric. For. Meteorol. 150, 501–509.
Masolele, R.N, De Sy, V., Herold, M., Marcos, D., Verbesselt, J., Gieseke, F., Mullissa, A. G., Martius, C., 2021. Spatial and temporal deep learning methods for deriving land-use following deforestation: a pan-tropical case study using Landsat time series. Remote Sens. Environ. 264, 112600.
Mallick, K., Jarvis, A., Wohlfahrt, G., Kiely, G., Hirano, T., Miyata, A., Yamamoto, S., Hoffmann, L., 2015. Components of near-surface energy balance derived from satellite soundings - Part 1: noontime net available energy. Biogeosciences. 12 (2), 433–451.
McCabe, M.F., Aragon, B., Houborg, R., Mascaro, J., 2017. CubeSats in hydrology: ultrahigh-resolution insights into vegetation dynamics and terrestrial evaporation. Water Resour. Res. 53, 10,017–10,024.
McVicar, T.R, Jupp, D.L.B, 2002. Using covariates to spatially interpolate moisture availability in the Murray–Darling Basin: a novel use of remotely sensed data. Remote Sens. Environ. 79, 199–212.
Mu, Q., Heinsch, F.A., Zhao, M., Running, S.W., 2007. Development of a global evapotranspiration algorithm based on MODIS and global meteorology data. Remote Sens. Environ. 111, 519–536.
Mu, Q.Z., Zhao, M.S., Running, S.W., 2011. Improvements to a MODIS global terrestrial evapotranspiration algorithm. Remote Sens. Environ. 115, 1781–1800.
Norman, J.M., Kustas, W.P., Humes, K.S., 1995. Source approach for estimating soil and vegetation energy fluxes in observations of directional radiometric surface-temperature. Agric. For. Meteorol. 77, 263–293.
Oishi, A.C., Oren, R., Stoy, P.C., 2008. Estimating components of forest evapotranspiration: a footprint approach for scaling sap flux measurements. Agric. For. Meteorol. 148, 1719–1732.
Penman, H.L., 1948. Natural evaporation from open water, bare soil and grass. Proc. R. Soc. Lond. Ser. A Math. Phys. Sci. 193, 120–145.
Perez-Priego, O., El-Madany, T.S., Migliavacca, M., Kowalski, A.S., Jung, M., Carrara, A., Kolle, O., Martin, M.P., Pacheco-Labrador, J., Moreno, G., Reichstein, M., 2017. Evaluation of eddy covariance latent heat fluxes with independent lysimeter and sapflow estimates in a Mediterranean savannah ecosystem. Agric. For. Meteorol. 236, 87–99.
Reichstein, M., Falge, E., Baldocchi, D., Papale, D., Aubinet, M., Berbigier, P., Bernhofer, C., Buchmann, N., Gilmanov, T., Granier, A., Grünwald, T., Havránková, K., Ilvesniemi, H., Janous, D., Knohl, A., Laurila, T., Lohila, A., Loustau, D., Matteucci, G., Meyers, T., Miglietta, F., Ourcival, J..M., Pumpanen, J., Rambal, S., Rotenberg, E., Sanz, M., Tenhunen, J., Seufert, G., Vaccari, F., Vesala, T., Yakir, D., Valentini, R., 2005. On the separation of net ecosystem exchange into assimilation and ecosystem respiration: review and improved algorithm. Glob. Change Biol. 11, 1424–1439.
Ren, S., He, K., Girshick, R., Sun, J., 2017. Faster R-CNN: towards real-time object detection with region proposal networks. IEEE Trans. Pattern Anal. Mach. Intell. 39, 1137–1149.
Rienecker, M.M., Suarez, M.J., Gelaro, R., Todling, R., Bacmeister, J., Liu, E., Bosilovich, M.G., Schubert, S.D., Takacs, L., Kim, G.K., Bloom, S., Chen, J.Y., Collins, D., Conaty, A., Da Silva, A., Gu, W., Joiner, J., Koster, R.D., Lucchesi, R., Molod, A., Owens, T., Pawson, S., Pegion, P., Redder, C.R., Reichle, R., Robertson, F. R., Ruddick, A.G., Sienkiewicz, M., Woollen, J., 2011. MERRA: nASA's modern-era retrospective analysis for research and applications. J. Clim. 24, 3624–3648.
Rumelhart, D.E., Hinton, G.E., Williams, R.J, 1986. Learning representations by back-propagating errors. Nature 323, 533–536.
Shang, K., Yao, Y., Liang, S., Zhang, Y., Fisher, J.B., Chen, J., Liu, S., Xu, Z., Zhang, Y., Jia, K., Zhang, X., Yang, J., Bei, X., Guo, X., Yu, R., Xie, Z., Zhang, L., 2021. DNN-MET: a deep neural networks method to integrate satellite-derived evapotranspiration products, eddy covariance observations and ancillary information. Agric. For. Meteorol. 308-309, 108582.
Shang, K., Yao, Y.J., Li, Y.F., Yang, J.M., Jia, K., Zhang, X.T., Chen, X.W., Bei, X.Y., Guo, X.Z., 2020. Fusion of five satellite-derived products using extremely randomized trees to estimate terrestrial latent heat flux over Europe. Remote Sens. 12.
Shen, H.F., Jiang, Y., Li, T.W., Cheng, Q., Zeng, C., Zhang, L.P., 2020. Deep learning-based air temperature mapping by fusing remote sensing, station, simulation and socioeconomic data. Remote Sens. Environ. 240.
Shirmard, H., Farahbakhsh, E., Müller, R.D., Chandra, R., 2022. A review of machine learning in processing remote sensing data for mineral exploration. Remote Sens. Environ. 268, 112750.
Shi, H.Y., Chen, J., Li, T.J., Wang, G.Q., 2020. A new method for estimation of spatially distributed rainfall through merging satellite observations, raingauge records, and terrain digital elevation model data. J. Hydro Environ. Res. 28, 1–14.
Shuttleworth, W.J., Wallace, J.S., 1985. Evaporation from sparse crops-an energy combination theory. Q. J. R. Meteorol. Soc. 111, 839–855.
Song, D.X., Wang, Z.H., He, T., Wang, H., Liang, S.L., 2022. Estimation and validation of 30m fractional vegetation cover over China through integrated use of Landsat 8 and Gaofen 2 data. Sci. Remote Sens. 6, 100058.
Su, Z., 2002. The Surface Energy Balance System (SEBS) for estimation of turbulent heatfluxes. Hydrol. Earth Syst. Sci. 6, 85–100.

Sun, J., Di, L.P., Sun, Z.H., Shen, Y.L., Lai, Z.L., 2019. County-level soybean yield prediction using deep CNN-LSTM model. Sensors 19.

Talsma, C.J., Good, S.P., Miralles, D.G., Fisher, J.B., Martens, B., Jiménez, C., Purdy, A.J., 2018a. Sensitivity of evapotranspiration components in remote sensing-based models. Remote Sens. 10 (1601), 1–28.

Talsma, C., Good, S.P., Jimenez, C., Martens, B., Fisher, J.B., Miralles, D.G., McCabe, M. F., Purdy, A.J., 2018b. Partitioning of evapotranspiration in remote sensing-based models. Agric. For. Meteorol. 260-261, 131–143.

Tang, R.L., Li, Z..L., Tang, B, 2010. An application of the Ts–VI triangle method with enhanced edges determination for evapotranspiration estimation from MODIS data in arid and semi-arid regions: implementation and validation. Remote Sens. Environ. 114, 540–551.

Tsagkatakis, G, Aidini, A, Fotiadou, K, Giannopoulos, M, Tsakalides, P, 2019. Survey of deep-learning approaches for remote sensing observation enhancement. Sensors 19, 3929. -.

Twine, T.E., Kustas, W.P., Norman, J.M., Cook, D.R., Houser, P.R., Meyers, T.P., Prueger, J.H., Starks, P.J., Wesely, M.L., 2000. Correcting eddy-covariance flux underestimates over a grassland. Agric. For. Meteorol. 103, 279–300.

Wagle, P., Bhattarai, N., Gowda, P.H., Kakani, V.G., 2017. Performance of five surface energy balance models for estimating daily evapotranspiration in high biomass sorghum. ISPRS J. Photogramm. Remote Sens. 128, 192–203.

Wang, K.C., Dickinson, R.E., 2012. A review of global terrestrial evapotranspiration: observation, modeling, climatology, and climatic variability. Rev. Geophys. 50.

Wang, K.C., Dickinson, R.E., Wild, M., Liang, S.L., 2010. Evidence for decadal variation in global terrestrial evapotranspiration between 1982 and 2002: 1. Model development. J. Geophys. Res. Atmos. 115.

Wei, Z., Wang, L., Jasechko, S., Lee, X., Yoshimura, 2017. Revisiting the contribution of transpiration to global terrestrial evapotranspiration. Geophys. Res. Lett.

Widlowski, J..L., Pinty, B., Lavergne, T., Verstraete, M.M., Gobron, N., 2006. Horizontal radiation transport in 3-D forest canopies at multiple spatial resolutions: simulated impact on canopy absorption. Remote Sens. Environ. 103, 379–397.

Wilson, K., Goldstein, A., Falge, E., Aubinet, M., Baldocchi, D., Berbigier, P., Bernhofer, C., Ceulemans, R., Dolman, H., Field, C., Grelle, A., Ibrom, A., Law, B.E., Kowalski, A., Meyers, T., Moncrieff, J., Monson, R., Oechel, W., Tenhunen, J., Valentini, R., Verma, S., 2002. Energy balance closure at FLUXNET sites. Agric. For. Meteorol. 113, 223–243.

Wu, H., Yang, Q., Liu, J., Wang, G., 2020. A spatiotemporal deep fusion model for merging satellite and gauge precipitation in China. J. Hydrol. 584, 124664.

Wulder, M.A., Loveland, T.R., Roy, D.P., Crawford, C.J., Masek, J.G., Woodcock, C.E., Allen, R.G., Anderson, M.C., Belward, A.S., Cohen, W.B., Dwyer, J., Erb, A., Gao, F., Griffiths, P., Helder, D., Hermosillo, T., Hipple, J.D., Hostert, P., Hughes, M.J., Huntington, J., Johnson, D.M., Kennedy, R., Kilic, A., Li, Z., Lymburner, L., McCorkel, J., Pahlevan, N., Scambos, T.A., Schaaf, C., Schott, J.R., Sheng, Y.W., Storey, J., Vermote, E., Vogelmann, J., White, J.C., Wynne, R.H., Zhu, Z, 2019. Current status of Landsat program, science, and applications. Remote Sens. Environ. 225, 127–147.

Yamaç, S.S, Todorovic, M, 2020. Estimation of daily potato crop evapotranspiration using three different machine learning algorithms and four scenarios of available meteorological data. Agric. Water Manag. 228, 105875.

Yang, Y., Shang, S., 2013. A hybrid dual-source scheme and trapezoid framework–based evapotranspiration model (HTEM) using satellite images: algorithm and model test. J. Geophys. Res. Atmos. 118, 2284–2300.

Yao, Y., Liang, S., Cheng, J., Liu, S., Fisher, J.B., Zhang, X., Jia, K., Zhao, X., Qin, Q., Zhao, B., Han, S., Zhou, G., Zhou, G., Li, Y., Zhao, S., 2013. MODIS-driven estimation of terrestrial latent heat flux in China based on a modified priestley–taylor algorithm. Agric. For. Meteorol. 171-172, 187–202.

Yao, Y.J., Liang, S.L., Fisher, J.B., Zhang, Y.H., Cheng, J., Chen, J.Q., Jia, K., Zhang, X.T., Bei, X.Y., Shang, K., Guo, X.Z., Yang, J.M., 2021. A novel NIR-red spectral domain evapotranspiration model from the Chinese GF-1 satellite: application to the Huailai agricultural region of China. IEEE Trans. Geosci. Remote Sens. 59, 4105–4119.

Yao, Y.J., Liang, S.L., Li, X.L., Chen, J.Q., Wang, K.C., Jia, K., Cheng, J., Jiang, B., Fisher, J.B., Mu, Q.Z., Grunwald, T., Bemhofer, C., Roupsard, O., 2015. A satellite-based hybrid algorithm to determine the priestley-taylor parameter for global terrestrial latent heat flux estimation across multiple biomes. Remote Sens. Environ. 169, 216–233.

Yao, Y.J., Liang, S.L., Li, X.L., Hong, Y., Fisher, J.B., Zhang, N.N., Chen, J.Q., Cheng, J., Zhao, S.H., Zhang, X.T., Jiang, B., Sun, L., Jia, K., Wang, K.C., Chen, Y., Mu, Q.Z., Feng, F., 2014. Bayesian multimodel estimation of global terrestrial latent heat flux from eddy covariance, meteorological, and satellite observations. J. Geophys. Res. Atmos. 119, 4521–4545.

Yao, Y.J., Liang, S.L., Li, X.L., Zhang, Y.H., Chen, J.Q., Jia, K., Zhang, X.T., Fisher, J.B., Wang, X.Y., Zhang, L.L., Xu, J., Shao, C.L., Posse, G., Li, Y.N., Magliulo, V., Varlagin, A., Moors, E.J., Boike, J., Macfarlane, C., Kato, T., Buchmann, N., Billesbach, D.P., Beringer, J., Wolf, S., Papuga, S.A., Wohlfahrt, G., Montagnani, L., Ardo, J., Paul-Limoges, E., Emmel, C., Hortnagl, L., Sachs, T., Gruening, C., Gioli, B., Lopez-Ballesteros, A., Steinbrecher, R., Gielen, B., 2017a. Estimation of high-resolution terrestrial evapotranspiration from Landsat data using a simple Taylor skill fusion method. J. Hydrol. 553, 508–526.

Yao, Y., Liang, S., Yu, J., Chen, J., Liu, S., Lin, Y., Fisher, J.B., McVicar, T.R., Cheng, J., Jia, K., Zhang, X., Xie, X., Jiang, B., Sun, L., 2017b. A simple temperature domain two-source model for estimating agricultural field surface energy fluxes from Landsat images. J. Geophys. Res. Atmos. 122, 5211–5236.

Yebra, M., Dennison, P.E., Chuvieco, E., Riaño, D., Zylstra, P., Hunt, E.R., Danson, F.M., Qi, Y., Jurdao, S., 2013. A global review of remote sensing of live fuel moisture content for fire danger assessment: moving towards operational products. Remote Sens. Environ. 136, 455–468.

Yuan, Q., Shen, H., Li, T., Li, Z., Li, S., Jiang, Y., Xu, H., Tan, W., Yang, Q., Wang, J., Gao, J., Zhang, L., 2020. Deep learning in environmental remote sensing: achievements and challenges. Remote Sens. Environ. 241, 111716.

Yuan, W., Liu, S., Yu, G., et al., 2010. Global estimates of evapotranspiration and gross primary production based on MODIS and global meteorology data. Remote Sens. Environ. 114 (7), 1416–1431.

Zamani Joharestani, M., Cao, C., Ni, X., Bashir, B., Talebiesfandarani, S., 2019. PM2.5 prediction based on random forest, XGBoost, and deep learning using multisource remote sensing data. Atmosphere 10.

Zhang, Y., Liang, S., Zhu, Z., Ma, H., He, T., 2022. Soil moisture content retrieval from Landsat 8 data using ensemble learning. ISPRS J. Photogramm. Remote Sens. 185, 32–47.

Zhao, M., Heinsch, F.A., Nemani, R.R., et al., 2005. Improvements of the MODIS terrestrial gross and net primary production global data set. Remote Sens. Environ. 95 (2), 164–176.

Zhao, W.L., Gentine, P., Reichstein, M., Zhang, Y., Zhou, S., Wen, Y.Q., Lin, C.J., Li, X., Qiu, G.Y., 2019. Physics-constrained machine learning of evapotranspiration. Geophys. Res. Lett. 46, 14496–14507.